

Selective electro-oxidation of glycerol over Co-based ZIF-67 derived catalyst



A thesis
submitted to
Indian Institute of Science Education and Research Pune in partial
fulfilment of the requirements for the BS-MS Dual Degree Programme
(2015-20)

by

Adarsh Koul
(Reg. No. 20151086)



Supervisor: Prof. Dr. Wolfgang Schuhmann

Anal. Chem. – Elektroanalytik & Sensorik

Gebäude NC 04/788

D-44780 Ruhr-Universität Bochum

Germany

March 2020

©Adarsh

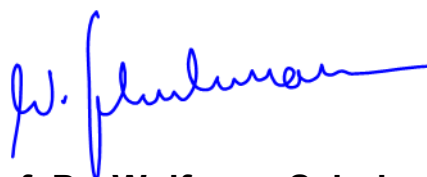
All rights reserved

Certificate

This is to certify that this dissertation entitled “**Selective electrooxidation of glycerol over Co-based ZIF-67 derived catalyst**” towards the partial fulfillment of the BS-MS dual degree programme at the **Indian Institute of Science Education and Research, Pune** represents study/work carried out by Adarsh Koul (Reg. No. 20151086) at **Ruhr University, Bochum** under the supervision of **Prof. Dr. Wolfgang Schuhmann, Chair, Analytical Chemistry** during the academic year 2019/20.



Adarsh Koul
BS-MS student
(Reg. No. 20151086)



Prof. Dr. Wolfgang Schuhmann
Analytical Chemistry
Ruhr University, Bochum

Date:

Place: Bochum, Germany

Committee: Chemistry

Name of Guide: Prof. Dr. Wolfgang Schuhmann

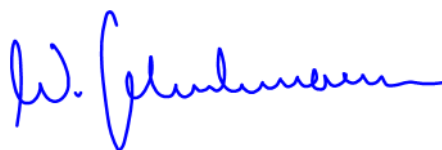
Name of TAC: Dr. Muhammed Musthafa. O. T

Declaration

I hereby declare that the matter embodied in the report entitled “**Selective electro-oxidation of glycerol over Co-based ZIF-67 derived catalyst**” are the results of the work carried out by me at the **Department of Analytical Chemistry, Ruhr University, Bochum**, under the supervision of **Prof. Dr. Wolfgang Schuhmann** and the same has not been submitted elsewhere for any other degree.



Adarsh Koul
BS-MS student
(Reg. No. 20151086)



Prof. Dr. Wolfgang Schuhmann
Analytical Chemistry
Ruhr University, Bochum

Date:

Place: Bochum, Germany

Dedicated to my loving parents

Ajay and Sunita

Acknowledgement

First and foremost, I would like to thank **Prof. Dr. Wolfgang Schuhmann** for providing me an opportunity to work under his supervision. He is always supportive and ensured that I integrated well in the research group where people from different ethnicities are working. I could not have imagined a better supervisor for my Master's studies.

Secondly, I would like to thank **Dr. Harshitha Barike Aiyappa** and **Dr. Nivedita Sikdar** for their incessant supervision throughout the course of the project. By sharing their scientific knowledge and expertise they walked me through the difficult times faced during the project.

I would also like to express my sincere gratitude to people who did characterization for my samples, Michael Braun for HPLC, Sandra Schmidt for SEM, Dr. Sabine Seisel for XRD, Steffen Cychy for IR, Dr. Nivedita Sikdar for NMR, Noushin Arshadi for BET, Thomas Quast for TEM.

I would like to thank all the lab members especially Michael, Swapnil, Simon, Vimanshu Ann Cathrin, Joao, and Dulce for all the fun stuff we did together and for helping me fight homesickness.

I would like to thank my family for their supporting phone calls and my friends for their group video chats which cheered me up every time.

Last but not the least, I would like to thank Lord Shiva for his blessings and prasad.

Contents

Chapter 1. Introduction.....	(12)
Chapter 2. State of the art.....	(14)
Chapter 3. Experimental section.....	(16)
3.1 Electrochemical techniques.....	(16)
3.1.1 Cyclic Voltammetry	
3.1.2 Chronoamperometry	
3.1.3 Impedance spectroscopy	
3.2 Synthesis.....	(18)
3.2.1 Synthesis of Co-based ZIF-67	
3.2.2 Pyrolysis	
3.2.3 Electrode preparation	
3.3 Cell Setups.....	(21)
3.3.1 Rotating disk electrode setup	
3.3.2 H-type cell setup	
3.3.3 Flow-through cell setup	
3.4 Instruments used.....	(25)
3.4.1 High-performance liquid chromatography	
3.4.2 In-situ infrared spectroscopy	
3.4.3 Nuclear magnetic resonance	
3.4.4 X-ray diffraction	
3.4.5 Scanning electron microscope	
3.4.6 Transmission electron microscope	
3.4.7 Brunauer-Emmett-Teller surface analysis	
Chapter 4. Results and discussion.....	(31)
4.1 Catalyst Screening.....	(31)
4.1.1 X-ray diffraction	

4.1.2 Scanning electron microscope	
4.1.3 Rotating Disk Electrode studies	
4.2 Surface analysis.....	(34)
4.2.1 Brunauer-Emmett-Teller surface analysis	
4.2.2 Transmission electron microscopy and elemental mapping	
4.3 Electrochemical analysis.....	(36)
4.3.1 H-cell	
4.3.2 Flow-through Cell	
4.4 Product analysis.....	(38)
4.4.1 In-situ infrared spectroscopy	
4.4.2 Nuclear magnetic resonance	
4.4.3 High-performance liquid chromatography	
Chapter 5. Conclusion.....	(42)
Chapter 6. Future outlook.....	(44)
References.....	(45)
Appendix.....	(47)

List of Figures

Label	Description	Page no.
Figure 1.1	Hydrogen cycle	12
Figure 2.1	Possible oxidation pathways and products on Pt-based catalyst for GOR	14
Figure 3.1	(a) Randles cell (b) Nyquist plot for Randles cell	17
Figure 3.2	ZIF-67 synthesis scheme	18
Figure 3.3	(a) Schematic representation of three zone tube furnace (b) Pyrolysis scheme	19
Figure 3.4	Rotating Disk electrode setup	21
Figure 3.5	H-type cell setup	22
Figure 3.6	Flow-through cell setup	23
Figure 3.7	Flow-through cell compartments	24
Figure 3.8	High-Performance Liquid Chromatography setup	25
Figure 3.9	In-situ Infrared setup schematic	26
Figure 3.10	NMR working principle	27
Figure 3.11	Schematic explaining Bragg's law	28
Figure 3.12	Schematic of a scanning electron microscope	29
Figure 4.1	(a) PXRD pattern for as synthesized ZIF-67 compared to simulated (b) PXRD pattern for Co/C-700, Co/C-800, Co/C-900 composites	31
Figure 4.2	SEM images (a) ZIF-67 (b) Co/C-700 (c) Co/C-800 (d) Co/C-900	32
Figure 4.3	Cyclic Voltammogram (a) CV1 and CV3 for three composites Co/C-700, Co/C-800 and Co/C-900 for GOR (b) OER for three composites Co/C-700, Co/C-800 and Co/C-900	33
Figure 4.4	Adsorption desorption isotherm (77 K, 1 bar) for Co/C-800	34

	composite	
Figure 4.5	(a) STEM image for Co/C-800 (b) HRTEM at 10 nm (c), (d) EDX elemental mapping at 100 nm and 10 nm.	35
Figure 4.6	(a) Cyclic Voltammogram comparing the activity of bare carbon electrode and drop-casted with Co/C-800 catalyst at scan rate 5 mA/cm ² (b) Chronoamperometry at 1.3 V vs. RHE	36
Figure 4.7	Electrolyte: 0.1 M glycerol in 1 M KOH (a) Cyclic voltammograms comparing activity in flow-through and H-type cell (b) Chronoamperometry at 1.4 V for 18 h in flow-through setup	37
Figure 4.8	(left)IR spectra at different potentials between 1.1 V to 1.8 V vs. RHE; (right) activity plot over time in the potential range 1.1 V to 1.8 V vs. RHE for 50 minutes	38
Figure 4.9	NMR spectra for (a) H-cell analyte after 12 H electrolysis at 1.3 V vs. RHE, (b) Flow-cell 1 h analyte (1.4 V vs. RHE), (c) Flow-cell 18 h analyte (1.4 V vs. RHE)	39
Figure 4.10	HPLC chromatograms for expected products and H-cell analyte after 12 h of chronoamperometry	40
Figure 4.11	HPLC chromatograms for analytes from flow-through setup at different time intervals	41
Figure 5.1	Possible reaction scheme for GOR over Co/C-800 catalyst	43
Figure A1	Calibration plots for concentration determination from HPLC chromatograms (a) FA, (b) GLA	47

List of Abbreviations

OER	Oxygen evolution reaction
DHA	Dihydroxyacetone
GLA	Glyceric acid
GLAD	Glyceraldehyde
LA	Lactic acid
MA	Mesoxalic acid
MOF	Metal-organic framework
AOR	Alcohol oxidation reaction
GOR	Glycerol oxidation reaction
CV	Cyclic voltammetry
CA	Chronoamperometry
DMSO	Dimethyl sulfoxide
OCP	Open circuit potential
KOH	Potassium hydroxide
ZIF-67	Cobalt-based zeolitic imidazolate framework
RDE	Rotating disk electrode
WE	Working electrode
GC	Glassy carbon
HPLC	High-performance liquid chromatography
In-situ IR	In-situ infrared spectroscopy
XRD	X-Ray diffraction
NMR	Nuclear magnetic resonance
SEM	Scanning electron microscopy
FCC	Face-centered cubic

Abstract

The increasing global energy demand has necessitated a lookout for newer renewable sources of energy that could replace or decrease the dependency of non-renewable sources i.e. fossil fuel. Hydrogen can be used as fuel and can be produced in various ways and one of the most effective means is by electrochemical water splitting. Hydrogen and oxygen are produced at the cathodic and anodic half-cells of the electrolyzer, respectively. However, due to the sluggish kinetics for the oxygen evolution reaction, the overall cost-effectiveness of the system decreases significantly. This could be overcome by using glycerol oxidation as the anodic half-cell reaction in the electrolyzer having a lower theoretical oxidation potential than water, cogenerating value-added products alongside. In this report, Co-based ZIF-67 (cobalt-based zeolitic imidazolate framework) a sub-category of metal-organic framework (MOF) has been pyrolyzed and used as an electrocatalyst for the glycerol oxidation reaction (GOR) where the ZIF is acting as a self-sacrificial template for a nitrogen-doped carbon matrix with metal nanoparticles dispersed within it. Morphological studies were carried out for the catalyst using techniques like SEM, TEM and PXRD. Different electrochemical cell setups like a rotating disk, H-cell and flow-through cells were used to investigate the activity and stability of the catalyst. Product selectivity for the catalyst was examined using techniques like HPLC, NMR and in-situ IR. Different products could be identified like formic acid, glyceric acid and carbonate with formic acid being the major product. Glyceric acid was also formed in substantial amounts.

1. Introduction

The depleting fossil fuels reserves and the number of pollutants produced while processing fossil fuels leaving behind a huge carbon footprint. Around 60 % of the total greenhouse gas production is due to fossil fuel combustion.^[1] As the population increases the energy requirements for the world are increasing at a huge pace. An alternative sustainable source of energy is the need of the hour.

From the past 20 years, hydrogen fuel has been considered as a substitute for the current non-renewable sources of energy.^[2] A hydrogen cycle with production sources and uses is shown in fig. (1.1).

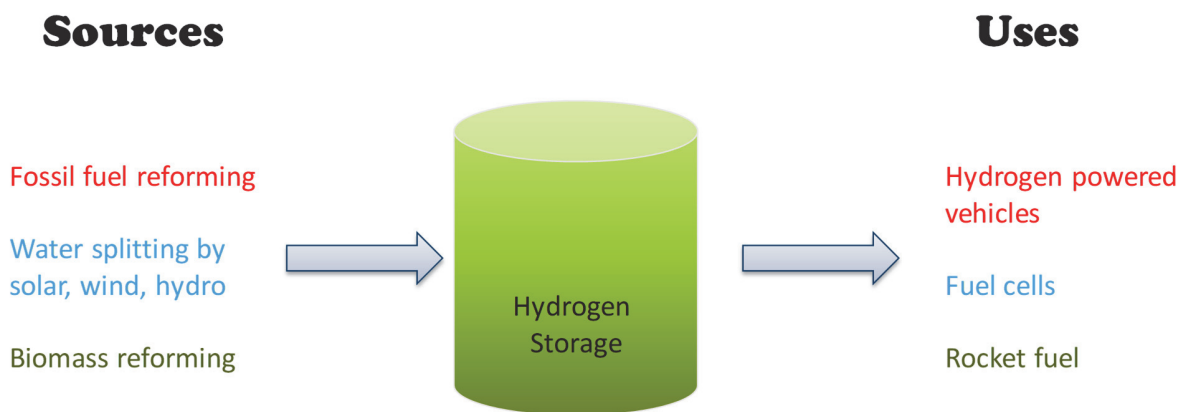


Figure 1.1: Hydrogen cycle recreated from Crabtree et al

For hydrogen fuel to be a success it should add more value to the market than fossil fuels. Cost-effective production is one of the major contributors to the hydrogen economy. Hydrogen fuel can be produced by a variety of techniques like steam reforming, electrolytic water splitting, fermentation and renewable liquid reforming.^[3] Among all these processes electrochemical water splitting occurs to be one the most promising method.^[3] High purity hydrogen and oxygen are produced at the two half cells: cathode and anode, respectively.^[4] The oxygen evolution reaction (OER) involves the sequential transfer of four electrons resulting in sluggish kinetics and high overpotential. Currently, the state of the art catalysts for the OER include IrO_2 and RhO_2

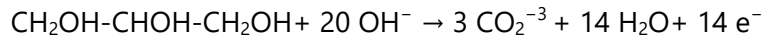
^[5] and other precious-metal-based catalysts. However, we are limited due to their scarcity, high cost and poisoning of catalyst surface due to carbon monoxide species.^[6]

Replacing the anode half-cell reaction (OER) with lower thermodynamic potential reactions and using earth-abundant metal-based catalysts could help us counter these limitations. The alcohol oxidation reaction (AOR) is one of the most studied anodic reactions in recent times. Methanol and ethanol are the widely used alcohols for AOR. However, they do not produce any valuable products after oxidation. Glycerol has a three-carbon backbone and three alcohol groups attached to them leading to a possibility of producing varied oxidation degree products.

Glycerol is one of the major byproducts of biodiesel production. For each ton of biodiesel produced 110 kg of glycerol are obtained.^[7] In 2016 the annual biodiesel production was 30.8 million m³ (Mm³). Biodiesel production is expected to rise at a rate of 4.5 % annually leaving behind tons of glycerol untreated.^[7] This motivates us to see glycerol as the fuel for future cogenerating products such as dihydroxyacetone (DHA), glyceric acid (GLA), glyceraldehyde (GLAD), lactic acid (LA), mesoxalic acid (MA) and many more having high commercial value.^[8]

2. State of the art

Glycerol oxidation is a multistep process and the complete oxidation to carbonate in alkaline media involves the transfer of 14 e⁻.



The first step of oxidation is base-catalyzed. Therefore, the use of alkaline media is expected to improve the kinetics of the reaction.^{[9][10]} Currently, the state of the art catalyst for GOR involves platinum, palladium, gold and other precious-metal-based catalysts. Platinum shows the lowest overpotential for GOR with an onset at 0.4 V vs. RHE (Reversible hydrogen electrode).^[11] The possible reaction pathway of GOR over Pt-based catalyst^[12] is shown in fig.(2.1).

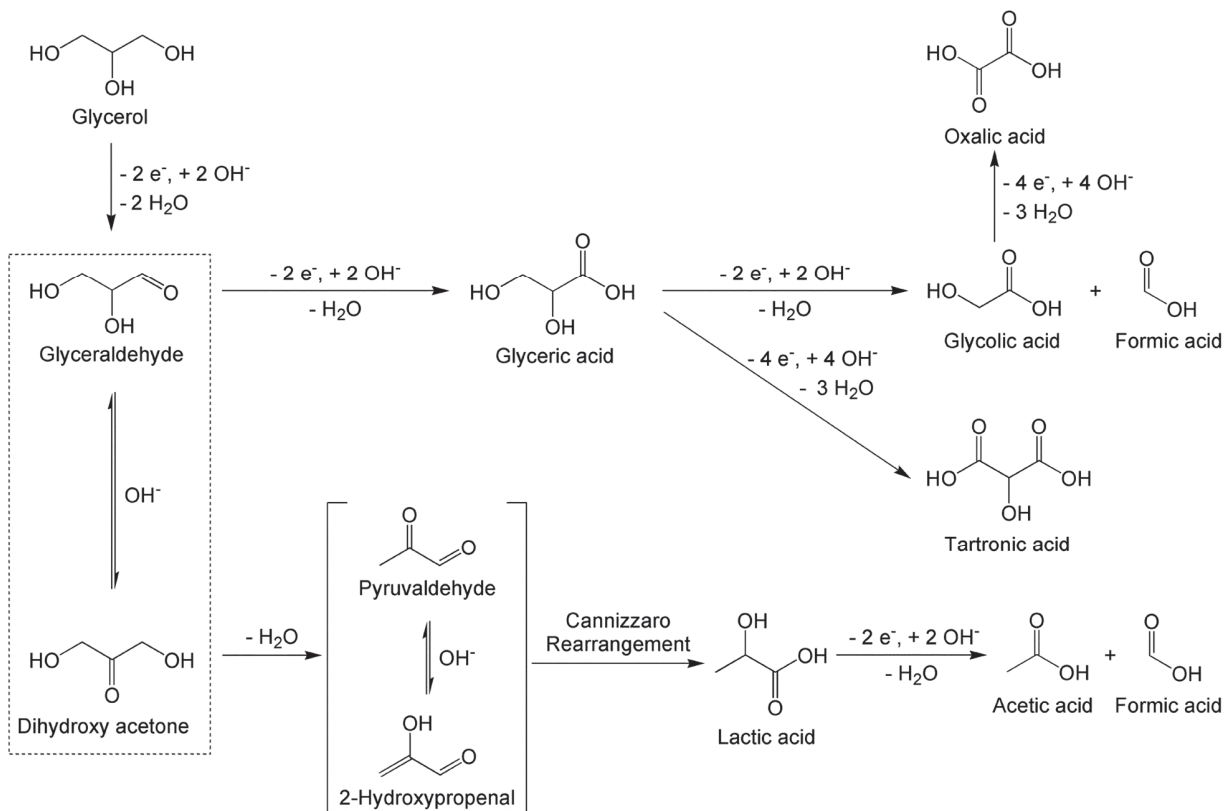


Figure 2.1: Possible oxidation pathways and products on Pt-based catalysts for the GOR

Recent reports have shown that the product selectivity on precious metal catalysts depends upon the potential applied during the catalysis.^[13,14] The primary hydroxyl group is oxidized at lower potentials (0.4 V - 0.6 V vs. RHE) forming products like GLAD, GLA and TA.^[11,15] Secondary oxidation products were only observed at higher potentials.^[16] C2/C1 products i.e. formic acid (FA), Glycolic acid (GA) and MA are formed from cleavage of one or two C-C bonds in GLA.^[17]

Fernandez *et al.* investigated the selectivity on platinum dispersed over multi-walled carbon nanotubes.^[18] Carrettin *et al.* have selectively oxidized glycerol to glyceric acid on gold-based in alkaline media.^[19] Garcia *et al.* used bismuth to modify platinum and found an increase in activity and selectivity for DHA.^[20]

However, the noble metals suffer from a high poisoning effect due to absorbed carbon monoxide species^[13,14] and their high cost has instigated the GOR research towards non-precious metal-based catalysts.

Transition metals are promising candidates as electrocatalyst because of their low cost and varied range of oxidation states.^[21] Amongst the transition metal catalysts, Ni-based catalyst has been an attractive contender for the GOR due to its abundancy, high resistance towards poisoning and high stability in alkaline media.^[15,22,23] However, the activity of the catalysts is not in par for commercial uses, as many of the Ni metal catalysts lead to cleavage of C-C bond even at low potentials leading to the formation of C2/C1 products like formate and carbonates with low commercial utility.^[23,24] Apart from nickel, copper and cobalt-based catalyst have also been studied for GOR.^[25] A recent work by Liu *et al.* investigated the effect of pH (in alkaline media) over CuO catalysts and it was observed that lower pH increases the selectivity for DHA.^[26]

The aim of this report is to design a non-precious metal-based catalyst for GOR which is easily scalable and usable for industrial purposes.

3. Experimental Section

Chemicals and materials used

S.No.	Chemical/Material	Purity (%)	Company Name
1.	Co(NO ₃) ₂ ·6H ₂ O	98	Sigma-Aldrich
2.	2-Methylimidazole	99	Sigma-Aldrich
3.	Methanol	100	VWR Chemicals
4.	Potassium Hydroxide	86.7	Fischer Chemicals
5.	Glycerol	99	Fischer Chemicals
6.	Sulfuric acid	95	Fischer Chemicals
7.	Sulfuric acid (HPLC grade)	98	Lichropur
8.	Dimethyl sulfoxide (DMSO)	99.9	Riedel-de Haen
9.	D ₂ O	99.9	Sigma-Aldrich
10.	Anion exchange membrane	-	Fumasep
11.	Carbon paper (H23, H23C2)	-	Freudenberg

3.1 Electrochemical Techniques

3.1.1 Cyclic voltammetry

Cyclic Voltammetry (CV) is an electrochemical technique in which current at the working electrode is measured as a function of potential applied between the working and the reference electrode. The counter electrode acts as a sink or source for the electrons in order to complete the circuit. The potential is varied linearly with time at a specific scan rate which was chosen to be 5 mV/s for all sets of experiments.

3.1.2 Chronoamperometry

Chronoamperometry (CA) is a long term current analysis technique, in which the current profile for an electrochemical reaction is monitored at a specific (constant) potential over time. All CA measurements were carried out using the three-electrode system.

3.1.3 Impedance Spectroscopy

Impedance spectroscopy was used to determine the uncompensated resistance in the system. The uncompensated resistance for a system can be affected by factors like the

shape of the cell, the distance between the working electrode (WE) and the reference electrode (RE) and the size of the counter electrode.^[27] Randles circuit (in fig.3.1) was used as the model circuit to interpret the impedance plots. Randles circuit is an electrical circuit consisting of a resistance (R_u = uncompensated resistance) in series with a capacitor (C_f = double-layer capacitance) and resistance (R_p = polarization resistance) in parallel. AC voltage was applied to have a specific frequency and the resulting current was used to measure the impedance. Similarly, a set of impedance values were collected over a range of frequencies i.e. 100 kHz – 1 kHz, 50 frequencies. The impedance from the resistor is independent of the frequency whereas it is inversely proportional for capacitance. Therefore, at low-frequency values all current passes through R_u and R_p giving a resultant impedance of $R_u + R_p$; and at higher frequencies, the impedance from the capacitor is negligible resulting in the final impedance value near to R_u . Randles circuit and Nyquist plot for a simulated Randles circuit are shown below.^[28] All impedance measurements were done in potentiostatic mode at a potential of 0 V vs. OCP (open circuit potential).

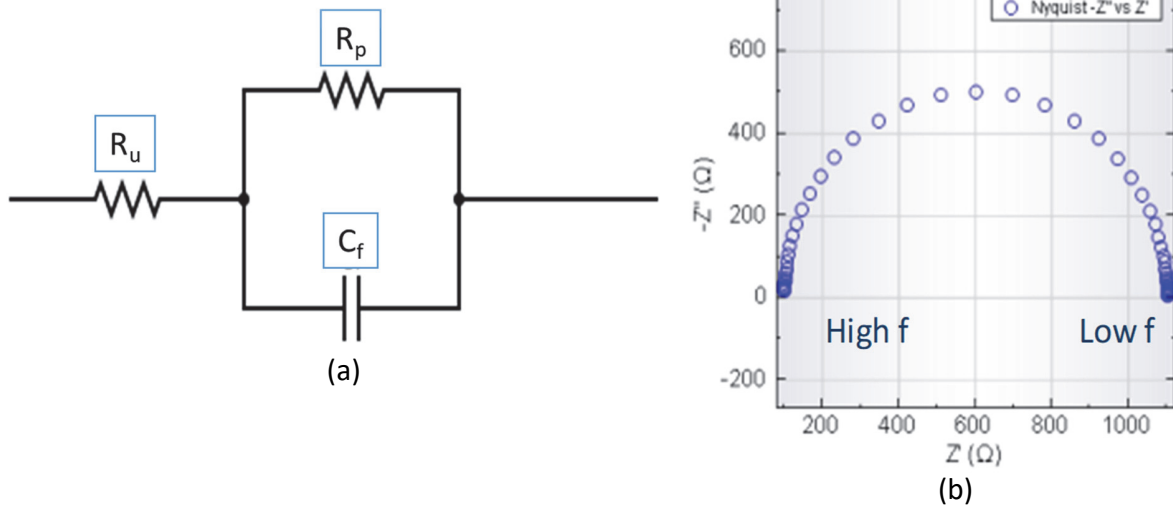


Figure 3.1: (a) Randles circuit; (b) Nyquist plot for Randles circuit^[28]

The potential values were converted to RHE and IR corrected using the following equation:

$$E_{RHE} = E_{Ag/AgCl/3M_KCl} + 0.59 \cdot pH - I \cdot R$$

(where I is the current and R is the uncompensated solution resistance)

The pH value for 1 M KOH was calculated using the following equation taking into consideration the activity of water (γ) in potassium hydroxide (KOH) as reported in the literature^[29].

$$\text{pH} = 14 + \log (\text{OH}^-) + \log \gamma$$

3.2 Synthesis

3.2.1 Synthesis of Co-based ZIF-67

Cobalt-based ZIF-67 was synthesized following a previously reported protocol.^[30] Metal and ligand precursors solutions were prepared by dissolving 5 mmol of $\text{Co}(\text{NO}_3)_2 \cdot 6\text{H}_2\text{O}$ and 40 mmol of 2-methylimidazole in 100 mL methanol each (metal to ligand molar ratio 1:8). The ligand solution was kept under stirring and the metal solution was added to it dropwise to obtain a purple-colored suspension. The suspension was allowed to stir for 1 h and was later centrifuged at 4700 rpm and washed with methanol till the supernatant was clear.

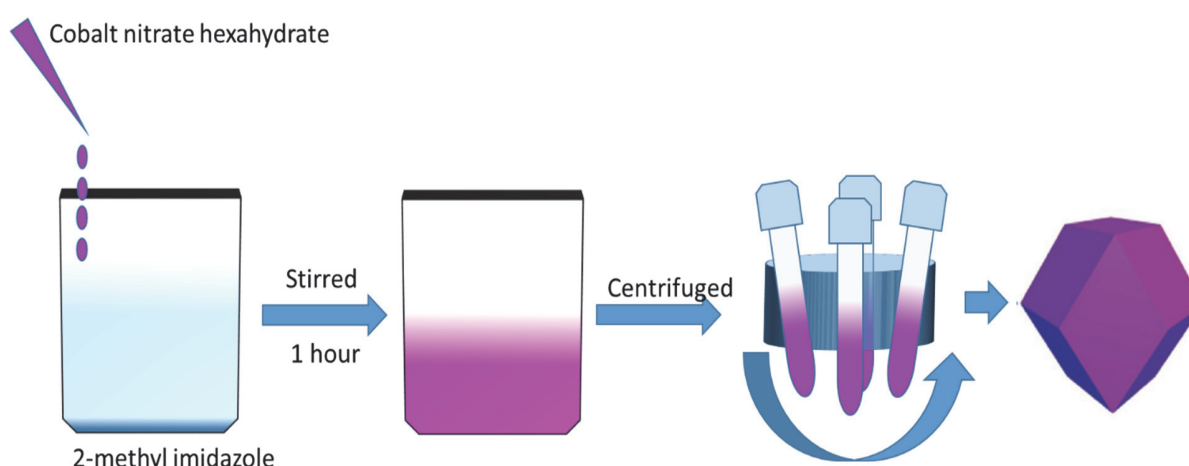


Figure 3.2: ZIF-67 synthesis scheme

3.2.2 Pyrolysis

A three-zone tube furnace was used for the carbonization of the as-synthesized ZIF-67 nanoparticles. The pyrolysis was carried out in reducing environment (10% H_2 + 90% Ar) with a heating rate of 10 K/min and carbonized for 4 h. Three different pyrolysis temperatures were chosen 700 °C, 800 °C, 900 °C resulting in three composites - Co/C-

700, Co/C-800, Co/C-900, respectively. The furnace was allowed to cool naturally to room temperature each time after pyrolysis.

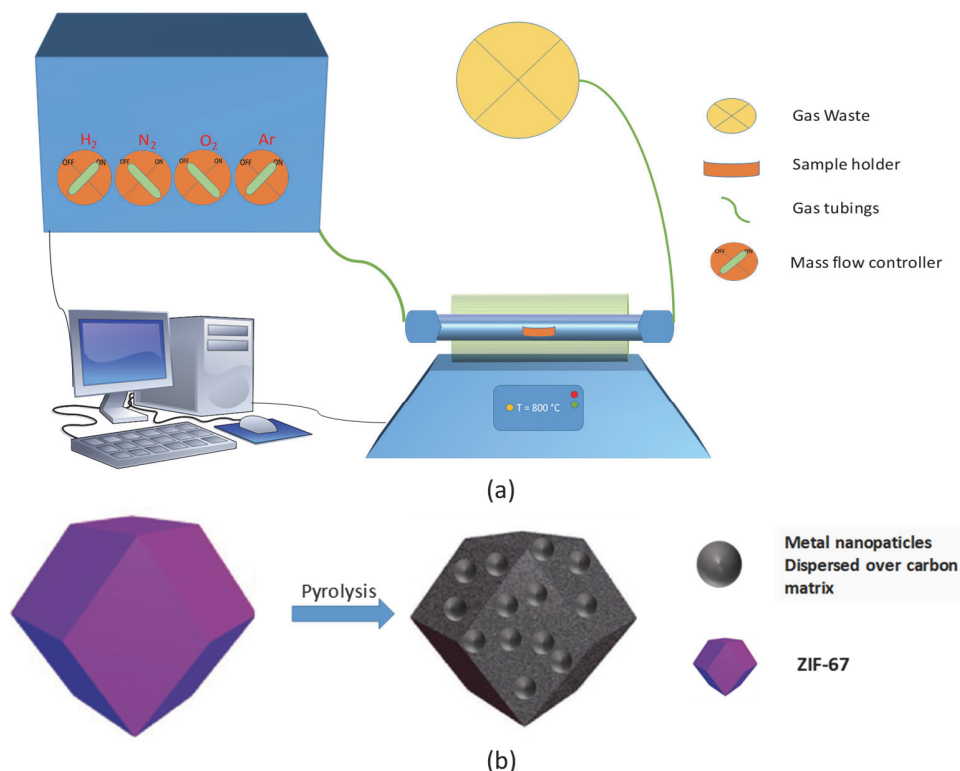


Figure 3.3: (a) Schematic representation of three-zone tube furnace (b) pyrolysis scheme

3.2.3 Electrode Preparation

Three different types of cell setups were used during the course of the project namely RDE (rotating disk electrode), H-type cell, flow-through cell and different working electrode materials were prepared by drop-casting catalyst ink prepared using the below-mentioned solvents:

Cell Type	Electrode material	Catalyst ink solvent	Type, electrode area	Final loading
RDE	Glassy carbon	Ethanol + water + Nafion (49:49:2)	Circular, 0.1134 cm ²	210 µg/cm ²
H-Type	Carbon paper H23	Ethanol + water + Nafion (49:49:2)	Square, 1 cm ²	1 mg/cm ²
Flow-through Cell	Carbon paper H23C2	Ethanol + Nafion (98:2)	Square, 1.44 cm ²	1 mg/cm ²

3.3 Cell Setups

3.3.1 RDE (Rotating Disk Electrode Setup)

All the RDE experiments were performed using an Autolab Potentiostat (Metrohm-Autolab PGSTAT302N). The cell setup consists of a three-electrode system. The working electrode (WE) is a cylindrical glassy carbon (GC) electrode covered with an insulating (Teflon) coating exposing a circular area for catalysis. Desired catalyst materials were drop-coated onto the GC electrode. The WE was rotated (1600 rpm) using a controller (in fig. 3.4) leading to forced convection of the electrolyte towards the catalyst increasing the mass transport. The platinum mesh was used as the counter electrode with a surface area larger than that of the WE. Ag/AgCl in 3 M KCl was used as a RE. CV analysis was carried out in 1 M Glycerol + 1 M KOH as an electrolyte at a scan rate of 5 mV/s. KOH electrolyte was also purified using a cation exchange column to remove metallic impurities.

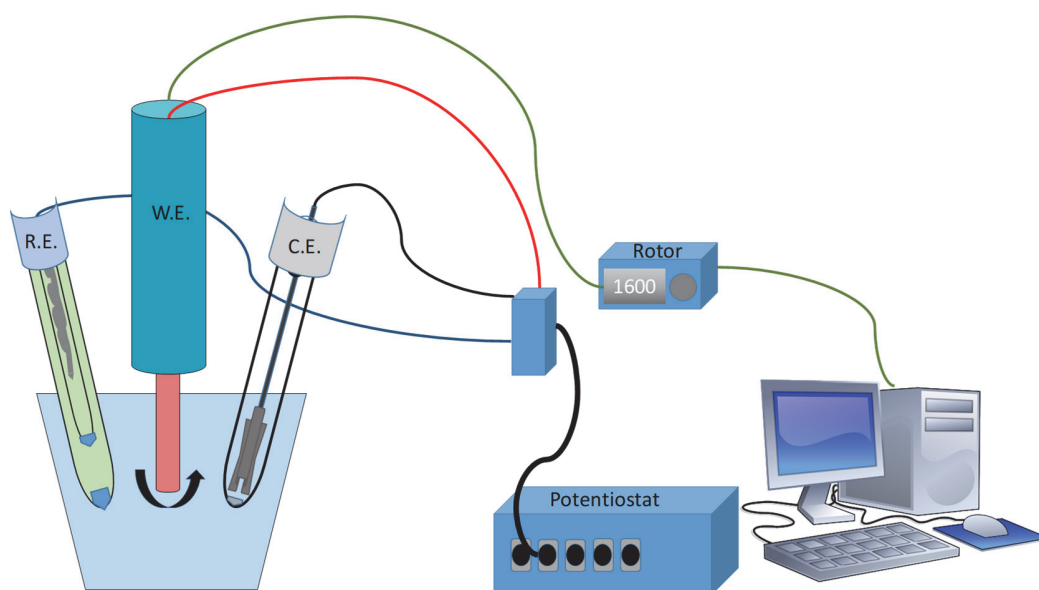


Figure 3.4: Rotating Disk electrode setup

3.3.2 H-Type Cell

The H-type cell is a two-compartment electrochemical cell consisting of anodic and cathodic half-cells separated by an anion exchange membrane (in fig. 3.5). Freudenberg H23 carbon paper was used as the support for the working electrode on

which the catalyst was drop-coated; a polished copper wire was used for connecting the WE to the potentiostat. The platinum mesh was used as the counter electrode; and homemade a Ag/AgCl in 3 M KCl as the reference electrode. FumaSep FAA-3-PK-130 was used as the anion exchange membrane. It was stored in 1 M KOH overnight before using it. The anodic compartment was filled with 5 mL of 0.1 M Glycerol in 1 M KOH and the cathodic compartment with 5 mL of 1 M KOH electrolyte. The electrolyte was purged with Argon (99.98 %) before using it. The anodic compartment was purged with Argon during the whole electro catalysis process. Chronoamperometry measurements were done at 1.3 V vs. RHE for 12 h with the aim of investigating the stability of the catalyst and as well as for product analysis. Electrolyte solutions were collected at the end of measurement and were immediately acidified using 0.51 M sulfuric acid and then stored in the refrigerator.

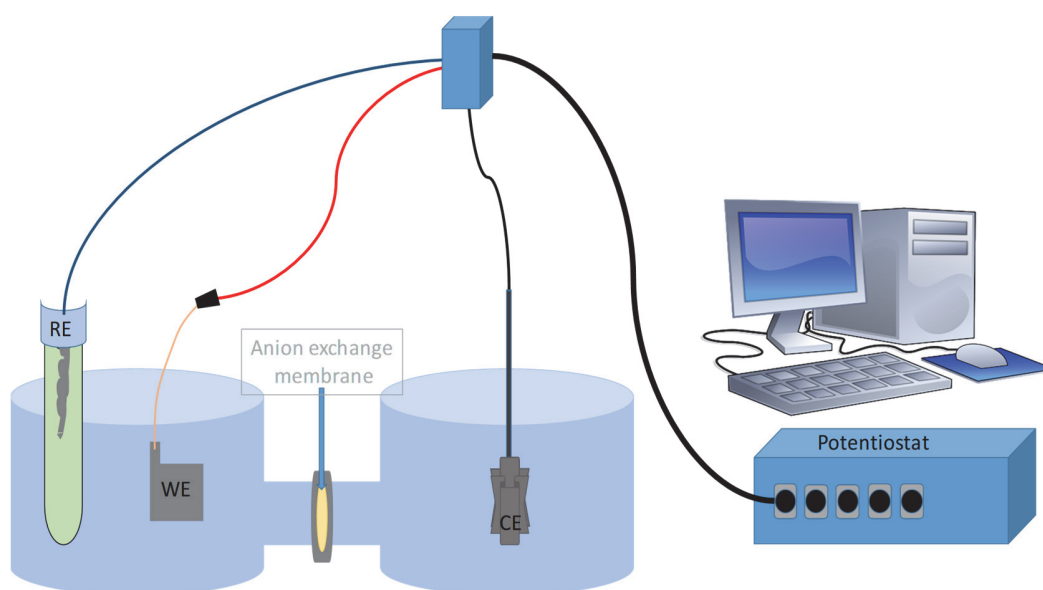


Figure 3.5: H-type cell setup

3.3.3 Flow-through cell

Flow-through cell setup comprised of a peristaltic pump, two electrolyte reservoirs (for cathodic and anodic compartments) and a flow-through cell (fig. 3.6, 3.7). In this setup, the electrolyte is allowed to flow over the surface of the catalyst providing forced convection that was lacking in the H-cell setup. Freudenberg H23C2 carbon paper (with a microporous layer) was used as the support (WE) on which the catalyst was drop-

coated. Ni-foam was used as the counter electrode and homemade Ag/AgCl in 3 M KCl as the reference electrode. FumaSep FAA-3-PK-130 was used as the anion exchange membrane separating the two half-cell compartments. CA measurements were carried out at potential 1.4 V vs. RHE. Electrolyte solutions were collected from the reservoirs during the measurements at different time intervals and were immediately acidified using 0.51 M sulfuric acid and then stored in the refrigerator. Acidification was done in order to prevent polymerization or other side reactions for possible aldehyde and alcohol products in alkaline media.^[31]

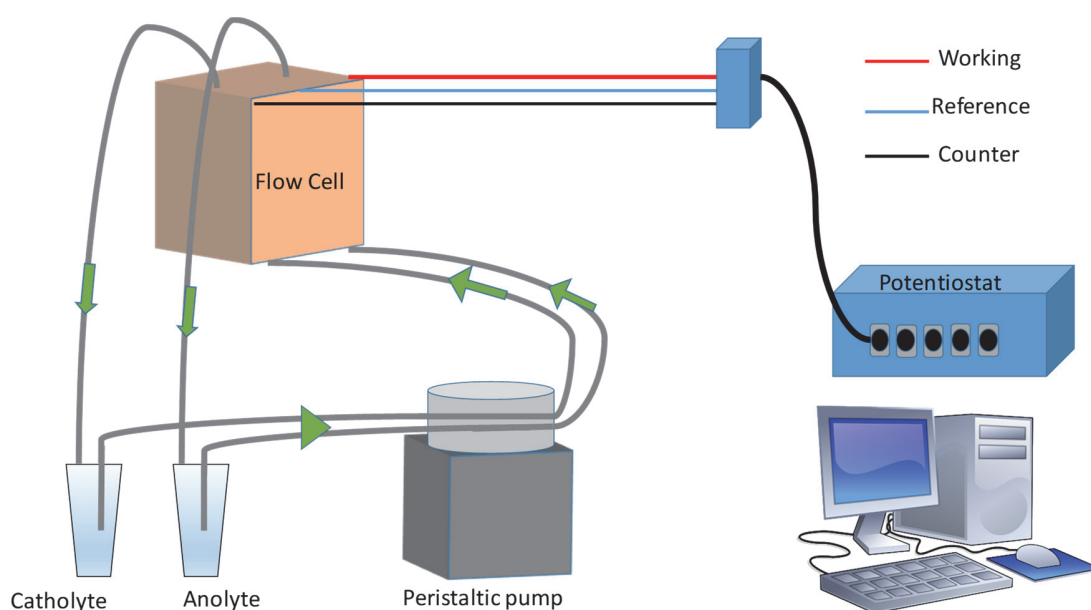


Figure 3.6: Flow-through cell setup

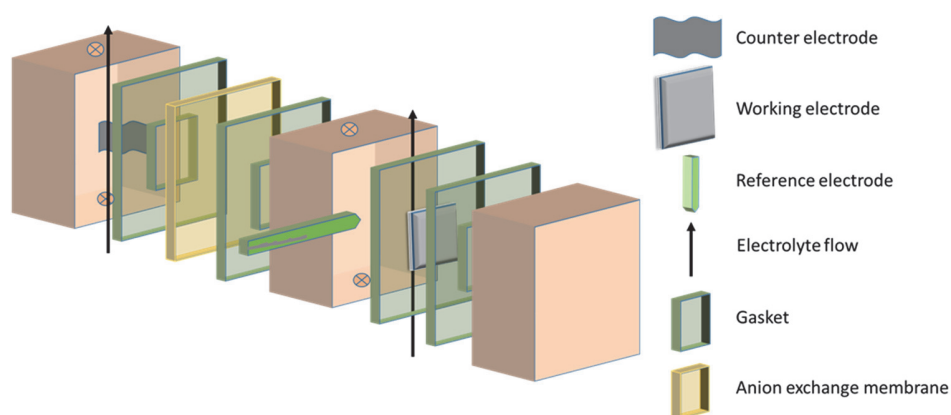


Figure 3.7: Flow-through cell compartments

3.4 Instruments used

3.4.1 HPLC (High-Performance Liquid Chromatography)

Chromatography is a technique of separating chemical mixtures based on their properties like polarity, size and charge. A conventional chromatography technique consists of a mobile phase, stationary phase, columns and the analyte. The analyte is loaded in the column (stationary phase) and the eluent (mobile phase) is allowed to run through the column and depending upon the interactions between the analyte and stationary phase the components of the mixture are eluted at different times resulting in separation. Liquid chromatography is used for separating mixtures in the liquid phase. HPLC is an improved form of liquid chromatography in which high pressure is applied to run the analyte through the column resulting in faster and better separation.

In our setup as shown in (fig. 3.8), an auto sampler was used for sample injection. Two columns (Acclaim OA, ICE-AS1 – separation based on pK_a values) were used in series, at a pressure of 60 bar and at temperature 30 °C controlled using an oven. 4 mM sulfuric acid was used as eluent with a flow rate of 0.5 mL/min. The separated compounds were detected using a refractive index detector. Product concentration was calculated by plotting concentration versus area under the curve for reference product chromatograms.

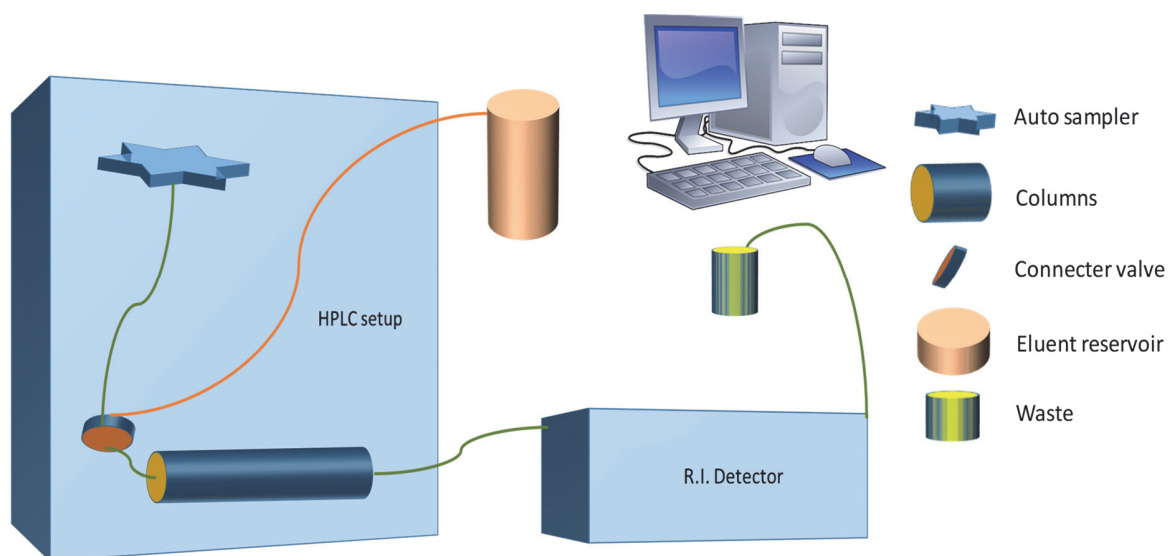


Figure 3.8: High-Performance Liquid Chromatography setup

3.4.2. In-situ IR (In-situ Infrared Spectroscopy)

IR spectroscopy works on the principle that molecules absorb light of specific frequencies which is resonant to the vibrational energy levels of the bond or the group of atoms. The vibrational energy is characteristic for each bond as it depends on the bond length and size of atoms. The evanescent wave i.e. energy radiated due to the relaxation of the molecule from excited vibrational state to the ground state is detected by the spectrometer. In-situ IR spectra were collected during the GOR using a three-electrode setup as shown in fig 3.9.

All spectra were recorded on BrukerTensor 27 FTIR spectrometer along with A530/P reflection unit combining a single bounce Ge half-sphere IRE in order to obtain sufficient IR intensity in the region of interest 4000 to 800 cm^{-1} .

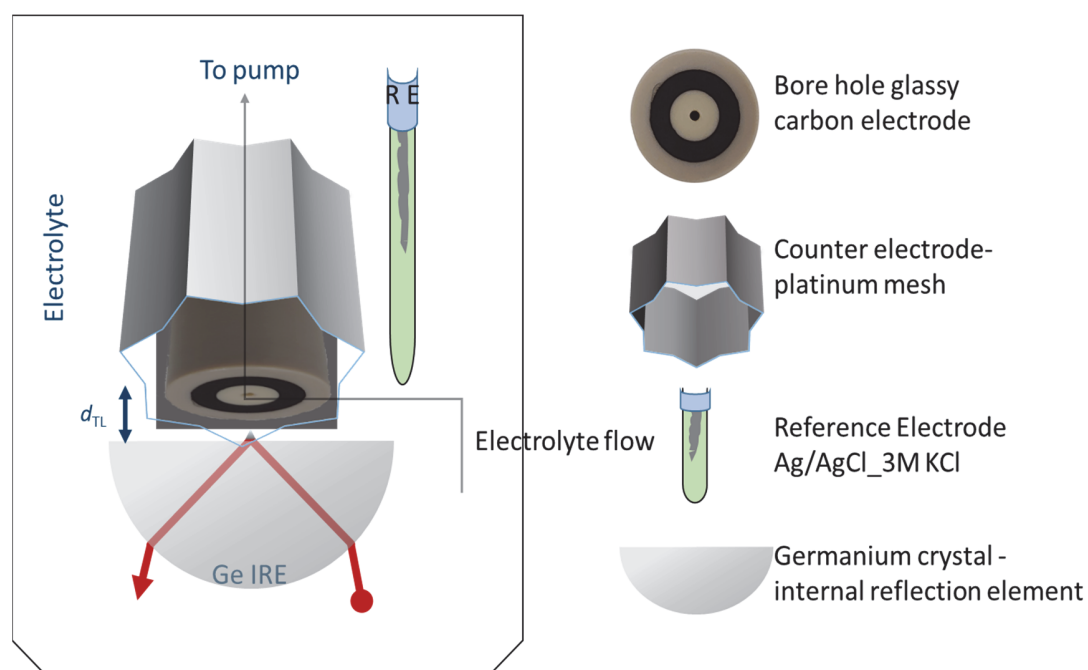


Figure 3.9: In-situ infrared setup schematic

3.4.3 NMR (Nuclear Magnetic Resonance)

Atoms having an odd number of protons or an odd number of neutrons or both can behave as magnets because of their spin and can exist in two energy levels one having a magnetic field in the direction of the applied magnetic field (ground state) and one

opposite (excited state), shown in fig. 3.10. An excitation can occur from ground level to excited state if energy resonating to this band-gap is applied. The band gap usually belongs to the radio frequency region. The band gap depends on the chemical environment of the atoms. Therefore, differently situated atoms would have different chemical shifts in the spectra. ^1H , ^{13}C , ^{15}N and ^{31}P are the most commonly used NMR nucleus. In this report, ^1H NMR spectra of the electrolyte (after electrolysis) were collected for the product analysis.

All NMR measurements were done on a Bruker DSX 400, (^1H resonance frequency: 400.13 MHz). NMR samples were prepared by adding 540 μL of analyte and 60 μL of internal reference solution (internal reference = 5 μL DMSO in 10 mL water, concentration = 7 mM). To assign the peaks, reference samples i.e. glycerol and expected products were prepared in the same way and were analyzed under NMR.

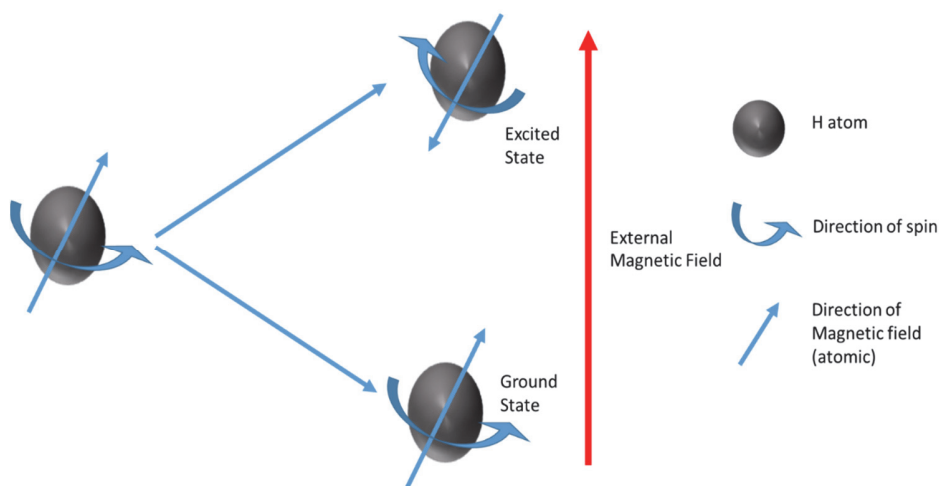


Figure 3.10: NMR working principle

3.4.4 XRD (X-Ray Diffraction)

XRD is a characterization technique used to determine the crystal planes, phase and unit cell dimensions for a crystal. As shown in the figure the X-rays incidents onto the crystal will get diffracted at the same angle as of incidence and would show constructive interference if the path difference between the diffracted rays is an integral multiple of the wavelength. Therefore, peaks can be observed at a specific angle of incidence. According to Braggs law $2d\sin\theta = n\lambda$ where d is the interplanar distance, θ is the angle

of incidence, λ is the wavelength and n is an integer. This gives us the relation between the angle of incidence and the plane width for a crystal.

XRD data were obtained using a Bruker D8 Discover X-ray diffractometer using a Cu K α radiation source ($\lambda = 1.5418 \text{ \AA}$) in the range of $2\theta = 5^\circ$ to 80° .

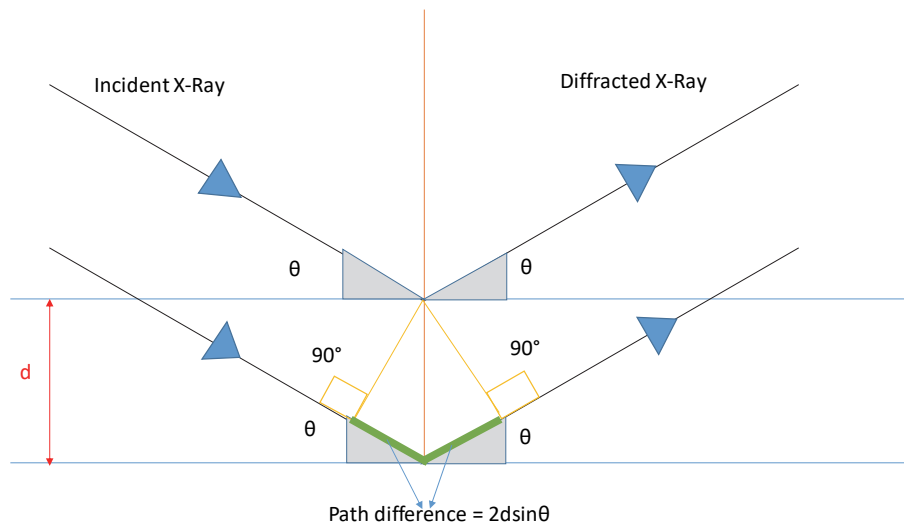


Figure 3.11: Schematic explaining Bragg's law

3.4.5 SEM (Scanning Electron Microscopy)

A beam of electrons is irradiated onto the sample surface. The interactions between the electrons and the sample generate secondary and backscattered electrons which are used for imaging in SEM. Secondary electrons are generated because of the inelastic collision between electrons and sample whereas backscattered electrons are originated due to elastic collisions. The schematic in fig. 3.12 shows the basic working principle of SEM. A small spatula tip of composites was dispersed in 1 mL of ethanol and sonicated for 15 minutes. 4 μL of the dispersion was drop-casted onto a silicon wafer and allowed to dry. The silicon wafers were later examined under SEM.

All SEM images were collected using a Quanta 3D FEG scanning electron microscope (FEI, Thermo Fisher Scientific, Germany).

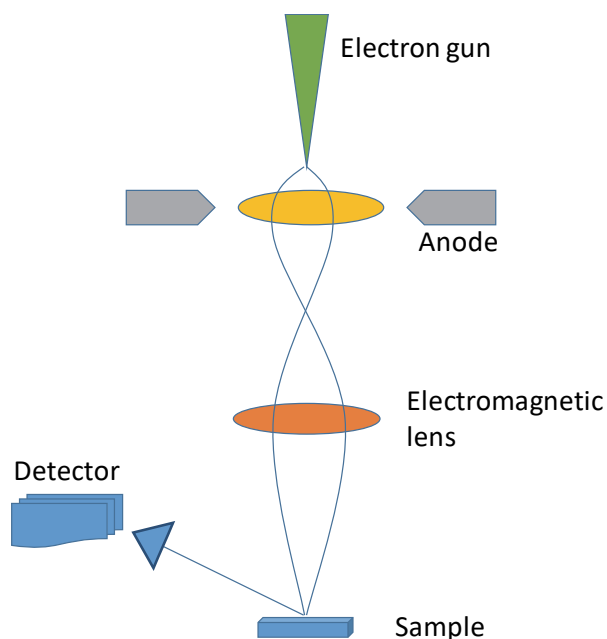


Figure 3.12: Schematic of a scanning electron microscope

3.4.6 TEM (Transmission Electron Microscopy)

TEM has a similar working principle as for the SEM but instead of detecting the scattered electrons TEM detects the transmitted electrons. Therefore, TEM provides information about the internal composition of the sample. All TEM imaging was performed on a JEOL microscope (JEM-2800) equipped with a Gatan OneView camera (4k×4k, 25FPS).

3.4.7 BET (Brunauer-Emmett-Teller) surface analysis

BET surface area analysis is done by calculating the amount of gas absorbed during the formation of a monolayer of gas over the surface of the analyte. BET measurements were carried out on Belsorp mini. The isotherms were collected using N₂ as adsorbate at 77 K and 1 bar.

4. Results and discussion

4.1 Catalyst screening

4.1.1 PXRD

The crystallinity for the as-synthesized Co-based ZIF-67 was confirmed using the PXRD technique. Comparing the PXRD data with the simulated sodalite structured ZIF-67(JCPDS:30-0443), all the peaks were precisely indexed having reflections at $2\theta=7.4^\circ$, 10.4° , 12.7° , 14.8° , 16.5° , 18.0° , 22.1° , 24.5° , 25.5° , 26.7° , 29.5° , 30.6° , 31.6° and 32.5° corresponding to planes (011), (002), (112), (022), (013), (222), (114), (233), (224), (134), (044), (334), (244) and (235). This confirmed the synthesis of ZIF-67 nanostructures. However, the peak intensities do not match perfectly with the theoretical intensities, this can be attributed to the defects in the crystal structure. The sharp peaks for the as-synthesized ZIF suggest high crystallinity and order. PXRD analysis for the catalysts composites Co/C pyrolyzed at three different temperatures (700°C , 800°C , 900°C) showed three distinct peaks at $2\theta = 44.2^\circ$, 51.6° and 76.0° corresponding to (111), (200) and (220) planes of the metallic cobalt in face-centered cubic (FCC) structure (JCPDS No. 15-0806). The increase in the sharpness of the peaks can be credited to the increase in the crystallinity of the cobalt nanoparticles on increasing the pyrolysis temperature.

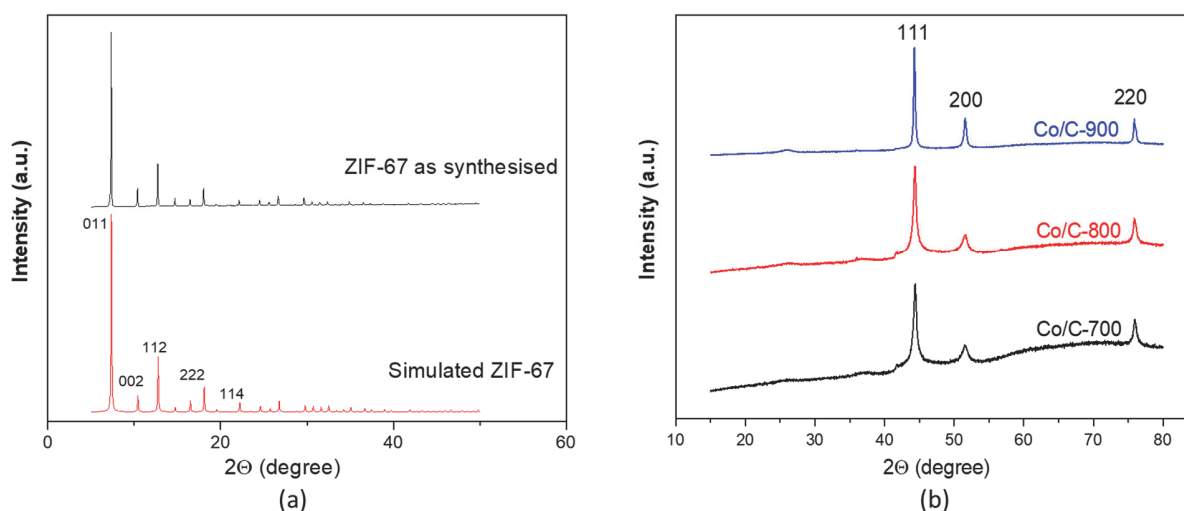


Figure 4.1: (a) PXRD pattern for as synthesized ZIF-67 compared to simulated (b) PXRD pattern for Co/C-700, Co/C-800, Co/C-900 composites

4.1.2 SEM

SEM images are indicative of the formation of rhombic dodecahedron-shaped nanoparticles, typical to the morphology of the ZIF-67 structure. The ZIF-67 particles exhibit a smooth surface with an average particle size of 250 nm. SEM images for the carbon composite pyrolyzed at 700 °C and 800 °C show that the nanoparticles retain the morphology of the pristine ZIF-67 MOF but with shrinkage and roughening of the faces which could be accounted to the heating effect during pyrolysis^[32]. However, for the sample pyrolyzed at 900 °C a collapse of the initial structure is observed which leads to agglomeration.

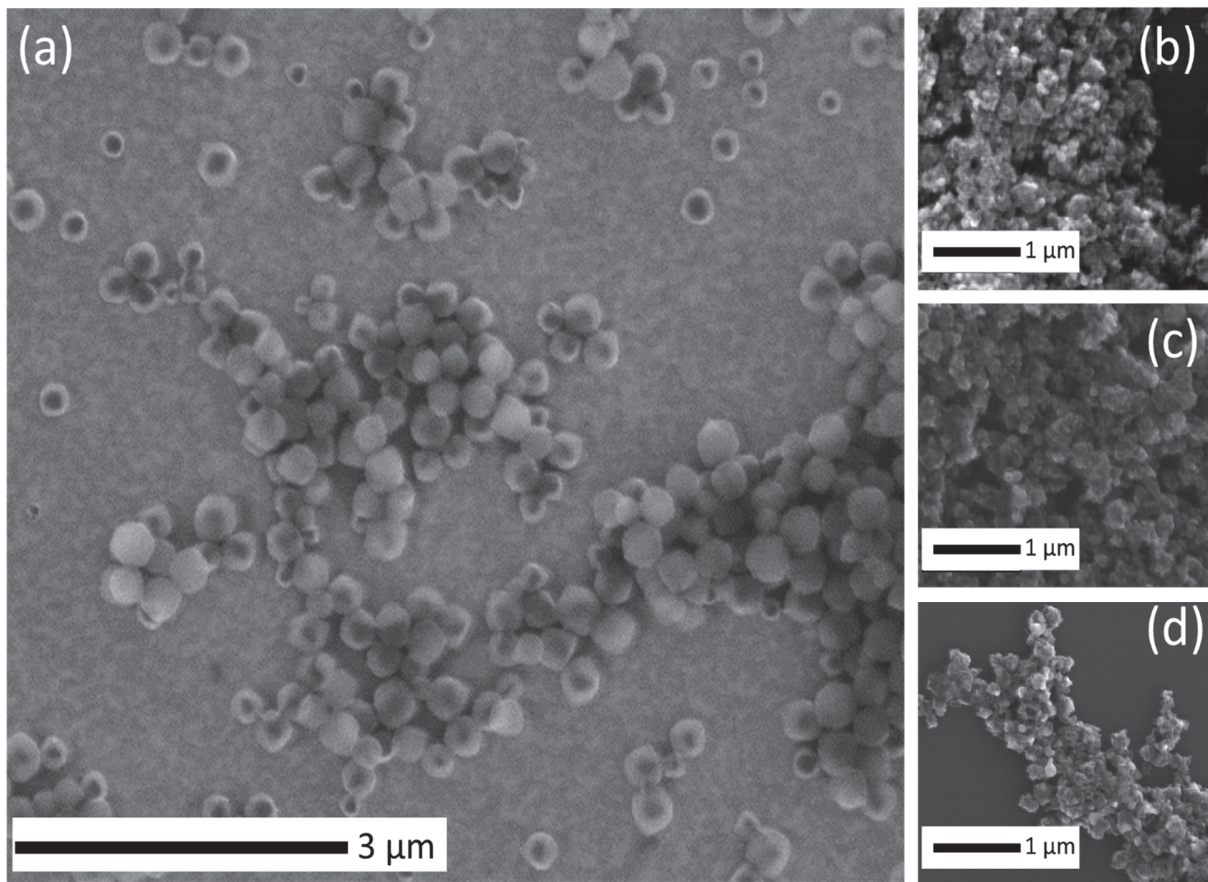


Figure 4.2: SEM images (a) ZIF-67 (b) Co/C-700 (c) Co/C-800 (d) Co/C-900

4.1.3 RDE studies

The three composites with different pyrolysis temperatures (700 °C, 800 °C and 900 °C) were analyzed for their activity towards glycerol oxidation using RDE experiments. 1 M glycerol + 1 M KOH was used as the electrolyte. CV studies were carried out using each composite. The Co/C-800 showed the lowest over-potential for GOR by reaching a current density of 10 mA/cm² at potentials as low as 1.28 V vs. RHE. The highest over-potential was observed for Co/C-700 composite. However, deactivation of the catalyst could be witnessed from cycle 1 to cycle 3 for each composite with the highest deactivation for the most active catalyst i.e. Co/C-800. The hysteresis in the CV can be accounted to the blockage of active sites by the intermediates and the products from GOR.^[33] The OER starts at potentials 1.6 V vs. RHE therefore at working potentials higher than 1.6 V the competing OER needs to be considered.^[34] Considering the lowest over-potential and highest activity of Co/C-800 towards GOR made it an eligible candidate for further analysis i.e. long-term electro-catalysis and product analysis.

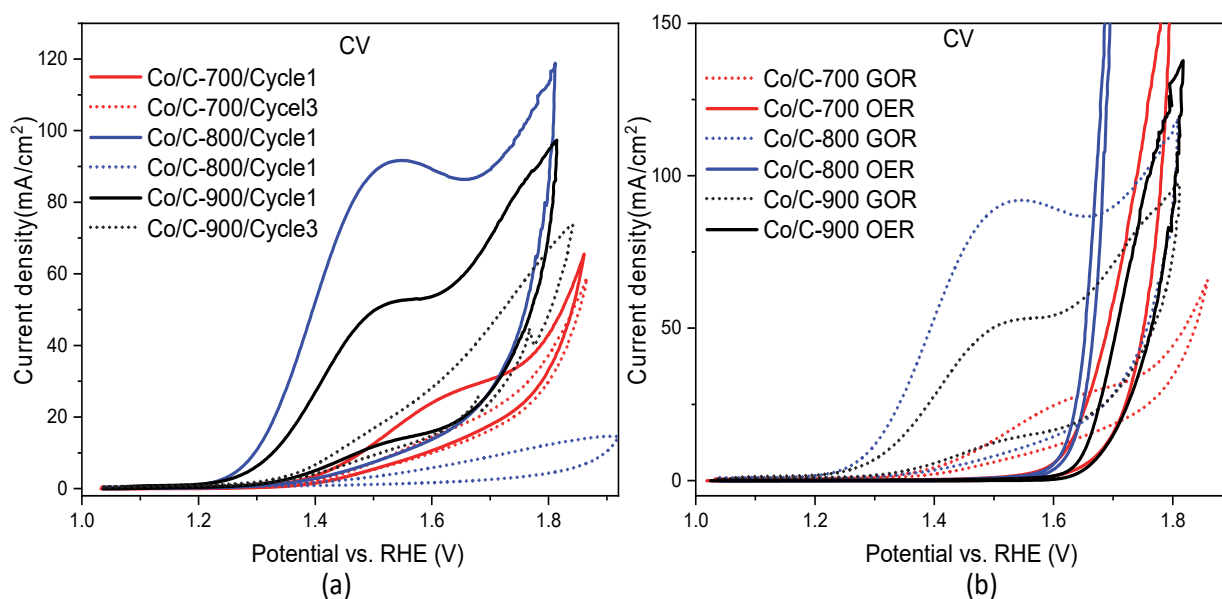


Figure 4.3: Cyclic voltammograms (a) CV1 and CV3 for three composites Co/C-700, Co/C-800 and Co/C-900 for GOR (b) OER for three composites Co/C-700, Co/C-800 and Co/C-900. Electrolyte - GOR: 1 M glycerol in 1 M KOH, OER: 1 M KOH, scan rate: 5 mV/s, 1600 rpm

4.2 Surface analysis

4.2.1 BET

The Co/C-800 composite was examined for BET surface area analysis. The surface area for the composite was 231 m²/g which concurs with the reported data.^[35] The adsorption and desorption isotherms suggest a mesoporous structure with capillary condensation. The Co/C-800 composite has an average pore diameter of 3.9 nm. Knowing that the kinetic diameter for glycerol is 6.2 Å, it can be inferred that the pores are easily accessible to the incoming glycerol molecule.

BET plot				
V _m			59.257	[cm ³ (STP) g ⁻¹]
BET surface area			257.91	[m ² g ⁻¹]
C			272.21	
Total pore volume(P/P ₀ =0.954)			0.2551	[cm ³ g ⁻¹]
Average pore diameter			3.9561	[nm]

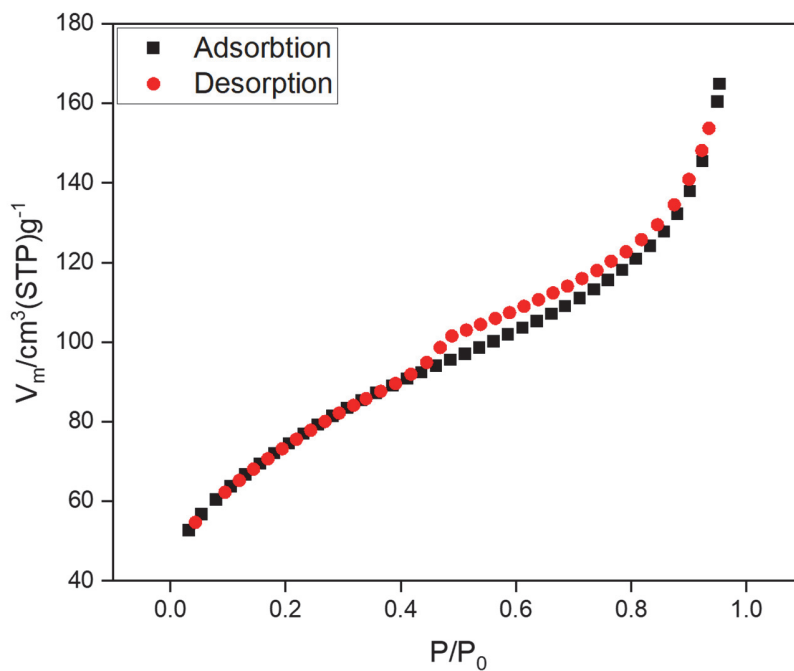


Figure 4.4: Adsorption-desorption isotherm (77 K, 1 bar) for Co/C-800 composite

4.2.2 TEM

Following the insight about the structure from the SEM images, TEM analysis for the Co/C-800 composite also suggests the initial rhombic dodecahedron-shape of the nanoparticles was retained after carbonization (fig 4.5 a). The average fringe width for the carbon structures was calculated to be 0.36 nm (fig 4.5 b). The fringe width for the cobalt nanoparticles (0.204 nm) agrees to the fringe width of (111) plane for simulated FCC lattice for metallic cobalt (JCPDS No. 15-0806). EDX mapping confirms the uniform distribution of cobalt nanoparticles over the carbon matrix (fig 4.5 c, d). TEM images at higher magnification also indicate that the metal nanoparticles are enclosed by graphitic structures (fig 4.5 d).

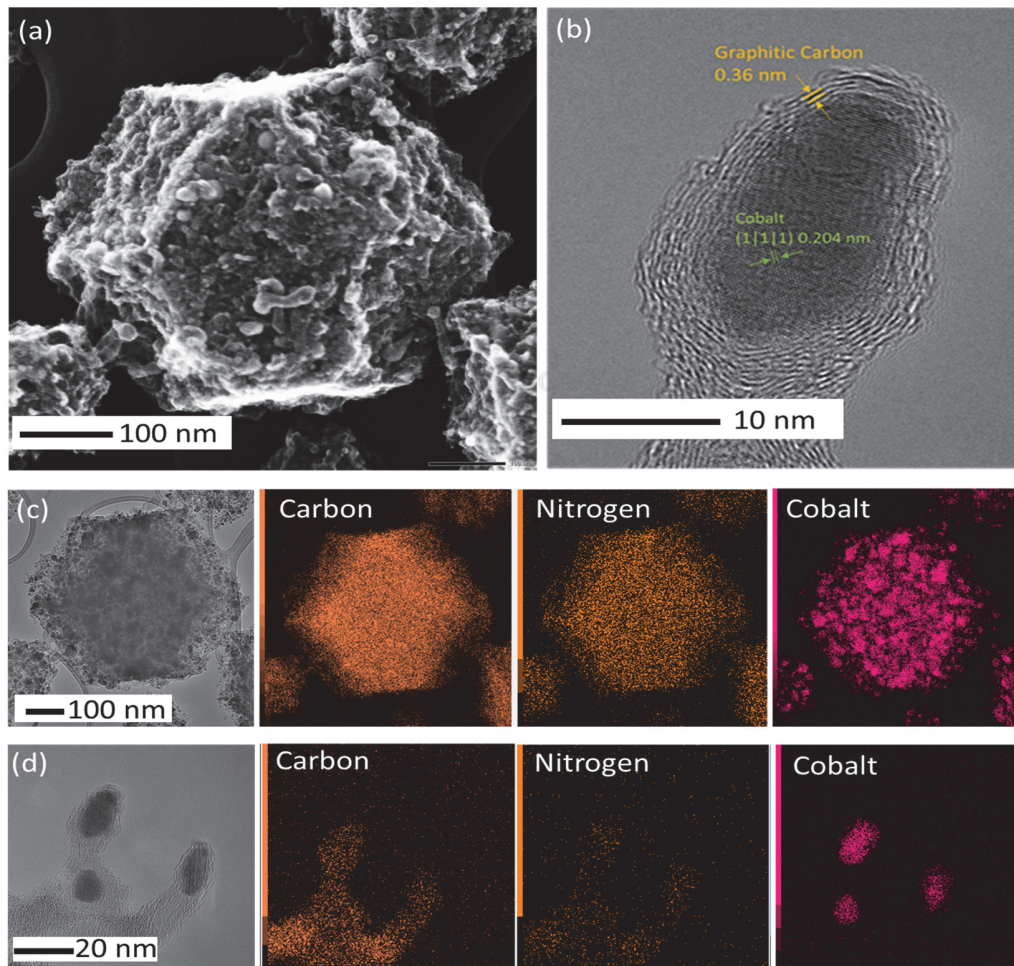


Figure 4.5: (a) STEM image for Co/C-800 (b) HRTEM at 10 nm (c), (d) EDX elemental mapping at 100 nm and 10 nm.

4.3 Electrochemical analysis

4.3.1 H-cell

All H-cell measurements were performed in 0.1 M glycerol + 1 M KOH electrolyte. CV analysis was done using the bare H23 carbon paper and the one with the catalyst in order to account for any background current due to carbon activity towards GOR. From fig. 4.6(a), carbon activity could be considered negligible as compared to the activity of the catalyst in the potential range of 1.2 V to 1.5 V vs. RHE. Chronoamperometry measurements were performed for the Co/C-800 coated electrode at a potential 1.3 V vs. RHE for 12 h (fig. 4.6-b). The current density values started from 5 mA/cm² and went down to 1.5 mA/cm² in a time duration of 30 minutes went further down to 0.5 mA/cm² in the next 11 h. The final analyte was studied for product characterization. The abrupt decay of the current density can be associated with the absence of convectional flow of the electrolyte towards the working electrode leading to the physisorption of intermediates over the catalyst surface.^[33] After 12 h of measurement, the analyte was acidified using the same volume of 0.51 M sulfuric acid as of the analyte in order to stabilize the aldehydes.^[31]

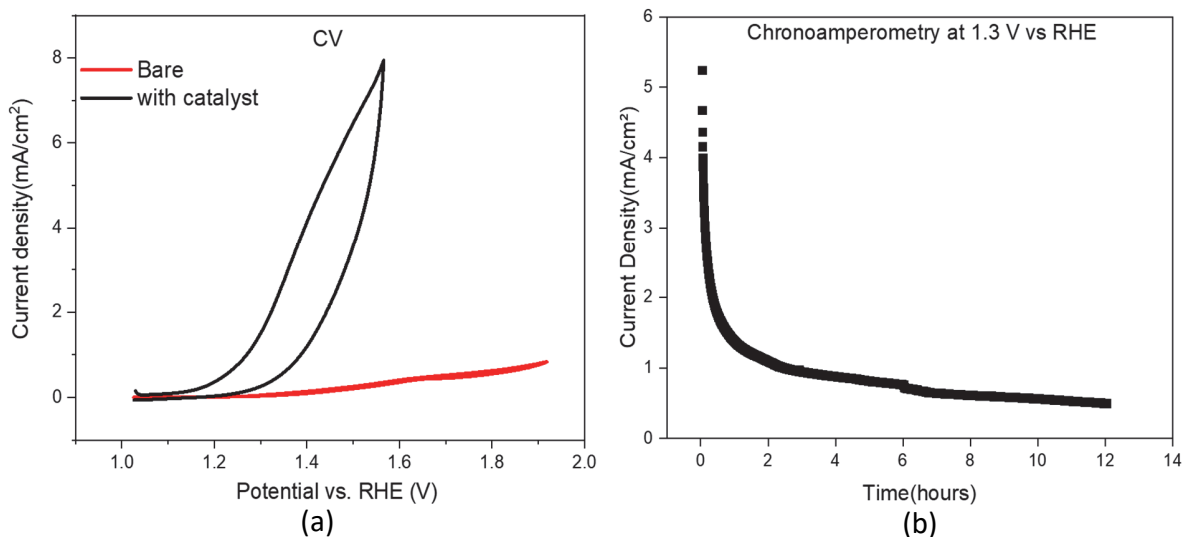


Figure 4.6: Electrolyte: 0.1 M glycerol in 1 M KOH (a) Cyclic voltammogram comparing the activity of bare carbon electrode and drop-casted with Co/C-800 catalyst at scan rate 5 mA/cm², (b) Chronoamperometry at 1.3 V vs. RHE

4.3.2 Flow-through cell

The limitations of the H-cell were the lack of forced convection and the inability to collect analyte samples during the electrocatalysis due to mechanical reasons. These limitations were overcome by the flow-through setup as shown in the fig. 3.7. On comparing the activity (CV) of the catalyst for the two setups – H-cell and flow-through cell, higher current densities could be achieved at lower potential values for the flow setup. This effectively explains the influence of the convective flow of the electrolyte towards the WE. Lower hysteresis in the flow-through setup-CV plot indicates the removal of physisorbed species (intermediates and products) due to continuous electrolyte flow. Even though the current density values increased for this setup the loss of activity over time could not be avoided. Chronoamperometry measurements were performed for a longer duration in order to increase product conversions. Chronoamperometry measurements were done for 18 h at a potential of 1.4 V vs. RHE. Analyte samples were collected manually during the course of the measurements at time intervals of 0 s, 30 s, 1 min, 2 min, 5 min, 10 min, 15 min, 20 min, 25 min, 30 min, 40 min, 50 min, 1 h, 1.5 h, 2 h, 4 h and 18 h. Analyte samples were immediately acidified using 0.51 M sulfuric acid, purged with argon and further analyzed under HPLC and NMR.

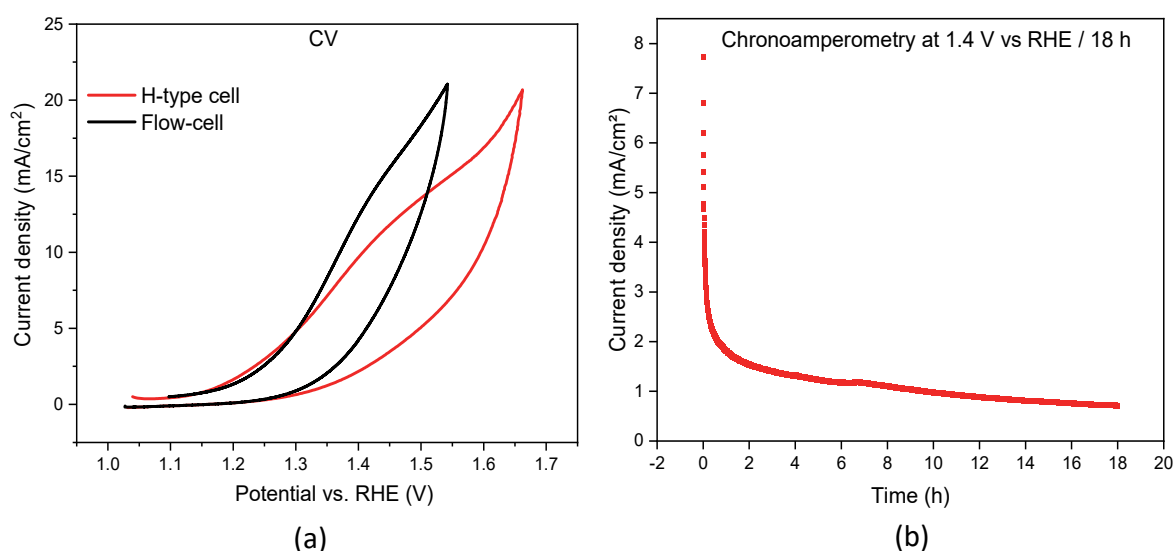


Figure 4.7: Electrolyte: 0.1 M glycerol in 1 M KOH (a) Cyclic voltammograms comparing activity in a flow-through and H-type cell (b) Chronoamperometry at 1.4 V for 18 h in flow-through setup.

4.4 Product analysis

4.4.1 In-situ infrared-spectroscopy

The IR spectra at different potentials are shown in fig. 4.8. IR spectra were collected in a potential range of 1.1 V to 1.8 V vs. RHE with each potential step of 100 mV. IR measurements were done for 6 minutes at each potential. IR bands for carbonate (1408 cm^{-1})^[36], FA and GLA (1573 cm^{-1})^[37] could be detected with the most prominent bands for FA at 1582 cm^{-1} , 1381 cm^{-1} and 1348 cm^{-1} .^[38] Peaks at 1064 cm^{-1} and 1098 cm^{-1} indicate GLAD as a possible product but with very low concentration.^[39] GLAD is the one-step oxidation product from glycerol and is very labile towards oxidation which could lead to immediate conversion to higher oxidation products and hence giving lower intensities for GLAD. The pattern of IR spectra over the range of potentials appears to be similar suggesting low or no dependence of selectivity over potential applied.

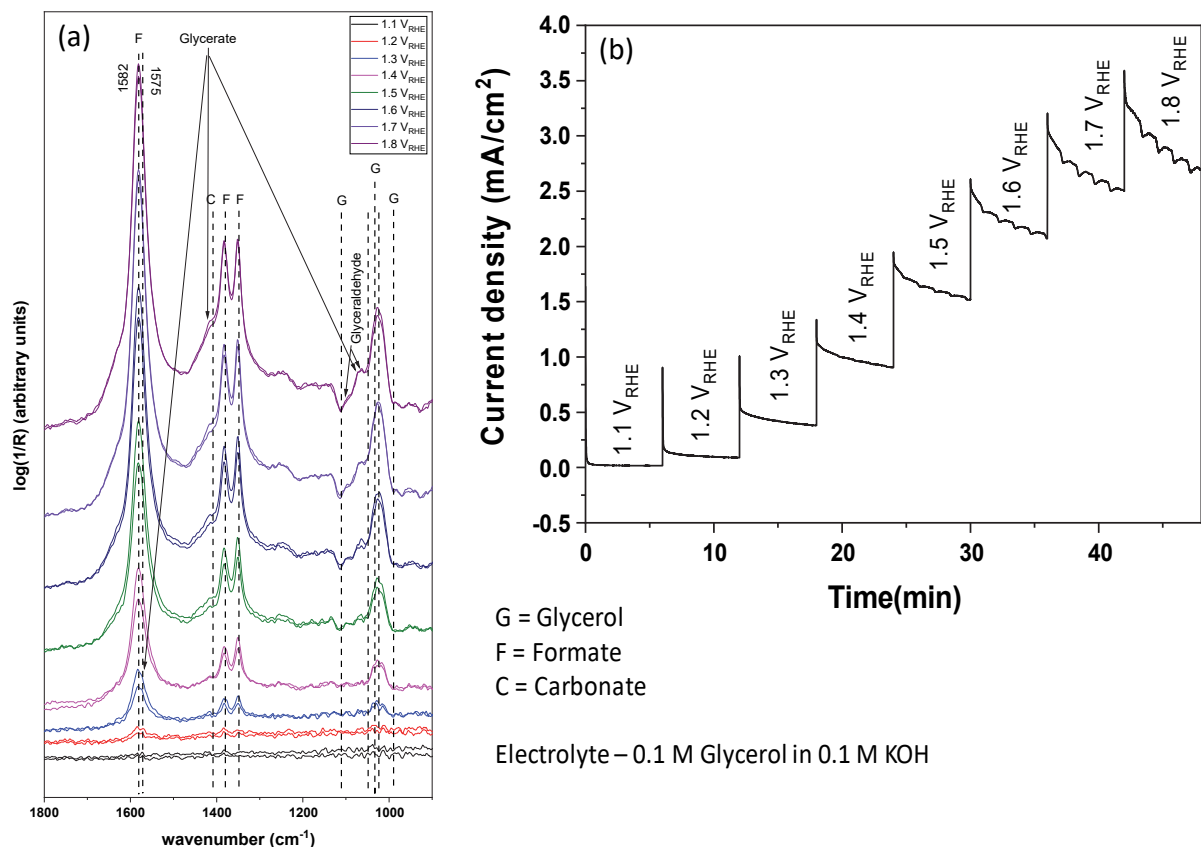


Figure 4.8: (a) IR spectra at different potentials between 1.1 V to 1.8 V vs. RHE; (b) activity plot over time in the potential range 1.1 V to 1.8 V vs. RHE for 50 minutes

4.4.2 NMR

The NMR spectra for both H-Cell and flow cell analytes (fig. 4.9) shows a singlet peak at 8.2 ppm and multiplet at 3.4 ppm. With the help of reference spectra, the multiplet peak can be assigned to glycerol and the singlet to FA. An expected increase in FA counts can be seen from flow-cell 1 h analyte to 18 h analyte as shown in fig 4.9 (b, c) glycerol products and intermediates like GLA and GLAD have a similar structure as glycerol, this could result in the merging of small products peaks with glycerol. A higher conversion of glycerol is required in order to detect all the possible products.

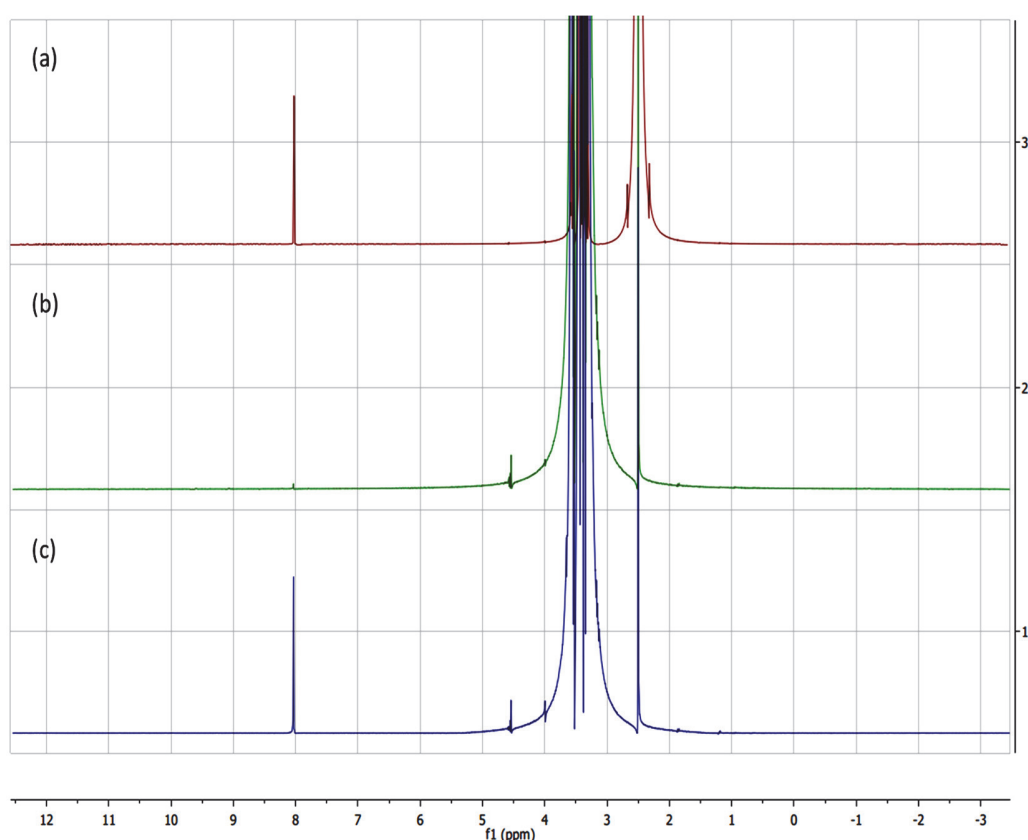


Figure 4.9 NMR spectra for (a) H-cell analyte after 12 h electrolysis at 1.3 V vs. RHE, (b) Flow-cell 1 h analyte (1.4 V vs. RHE), (c) Flow-cell 18 h analyte (1.4 V vs. RHE)

4.4.3 HPLC

A set of expected product solutions and glycerol were initially run through HPLC for referencing. As for NMR few of the glycerol derived products and intermediates could

not be resolved because of their similar pK_a values and structure which led to similar retention times. The HPLC chromatogram for the H-cell samples showed multiple peaks with retention times overlapping with the references glycerol (21 min.), GLA (19 min.), FA (23.3 min.), acetate (25.1 min.), and possible formaldehyde (21.8 min.) and with the highest intensity for the FA peak. However, few other peaks with relatively smaller intensities were observed within the retention times of 16-18 minutes which could not be identified. FA concentration in the analyte was 11 mM.

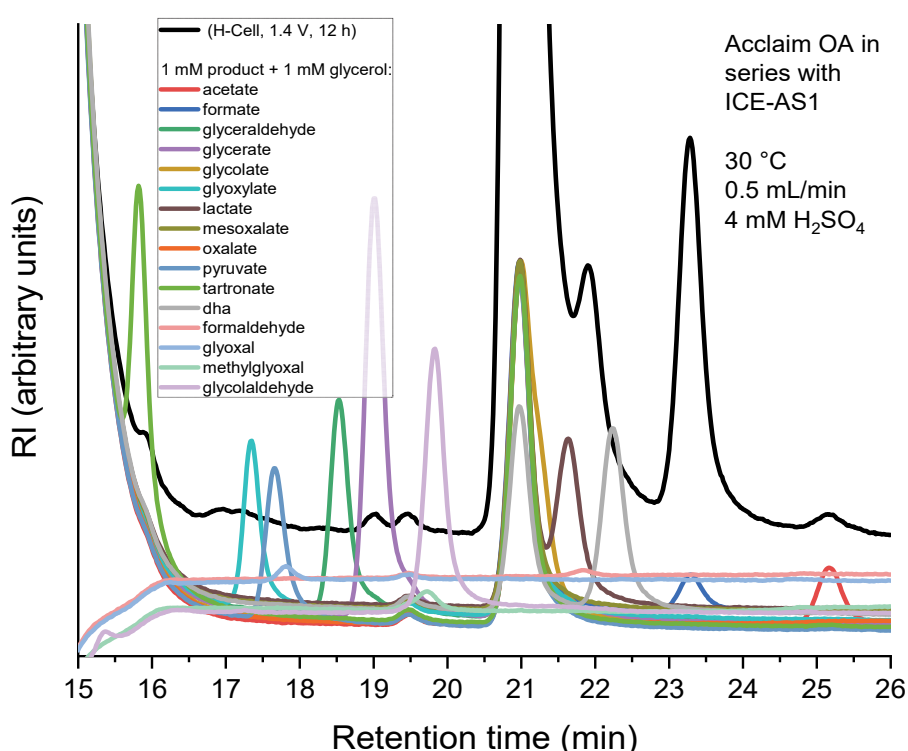


Figure 4.10: HPLC chromatograms for expected products and H-cell analyte after 12 h of chronoamperometry

The HPLC chromatograms for the flow-cell analytes showed an expected decrease in the glycerol peak intensity with time as it gets converted to products. A gradual increase in the GLA, FA, and formaldehyde peak intensities can be observed over time. Comparing the relative intensities of GLA and FA in H-cell and flow-through cell (18 h) analyte, it can be observed that higher GLA is produced during flow-through experiments which could be because of the flow of electrolyte so that glycerol molecules

spend less time over the catalyst and hence less prone to further oxidation. The FA to GLA ratio after 4 and 18 h of electrolysis, was 40:1 and 20:1 respectively. Therefore, at the initial stage of electrolysis, more FA is produced than GLA. This could be because of the higher activity of the catalyst in the beginning and hence could break the C-C bond in glycerol easily. However, after the deactivation of the catalyst, primary oxidation was favoured more than before and lead to higher conversion towards GLA.

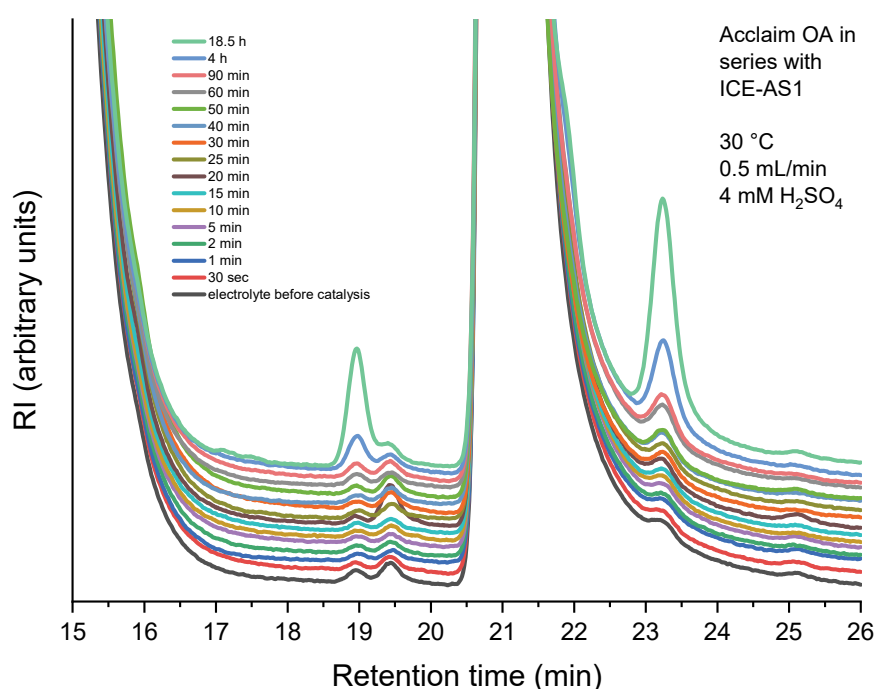


Figure 4.11: HPLC chromatograms for analytes from flow-through setup at different time intervals at 1.4 V vs. RHE

5. Conclusion

Co-based ZIF-67 nano-sized MOF was prepared using a one-pot synthesis method. The as-synthesized ZIFs were pyrolyzed at three different temperatures 700 °C, 800 °C, 900 °C. Initial screening of the catalysts reveals higher GOR activity of the Co/C-800 composite with an overpotential of 1.28 V vs. RHE (at 10 mA/cm²). Co/C-800 composite was therefore chosen for further studies. Material characterization techniques like SEM, TEM and PXRD confirmed the synthesis of the rhombic dodecahedron-shaped ZIF nanoparticles. TEM analysis for the Co/C-800 composite asserted the formation of

cobalt nanoparticles with FCC lattice enclosed by graphitic carbon structure. The formation of FCC structured cobalt nanoparticles was further confirmed by PXRD analysis. BET surface analysis suggested the formation of a mesoporous structure with an average pore diameter of 3.9 nm which implies that the pores are easily accessible to the incoming glycerol molecules having an average kinetic diameter of 6.2 Å. In-situ IR studies suggested the formation of FA with the most prominent peak and the probable presence of glyceraldehyde and glyceric acid. For higher conversion to the product, chronoamperometry studies were done on h-type and flow-through cell setup. The analytes were later processed for product characterization under NMR and HPLC. NMR studies for H-cell and flow-through cell analyte showed FA as the only detectable product. HPLC product characterization for H-cell analyte indicated the presence of formaldehyde, GLA, acetate in lower concentrations. However, the flow-cell setup analyte showed a considerable amount of GLA production. This can be attributed to the lower retention time of glycerol over the catalyst due to the flow of the electrolyte. A possible reaction scheme could be drawn based on the possible products as identified using different characterization techniques has been shown in fig. 5.1.

Possible reaction scheme

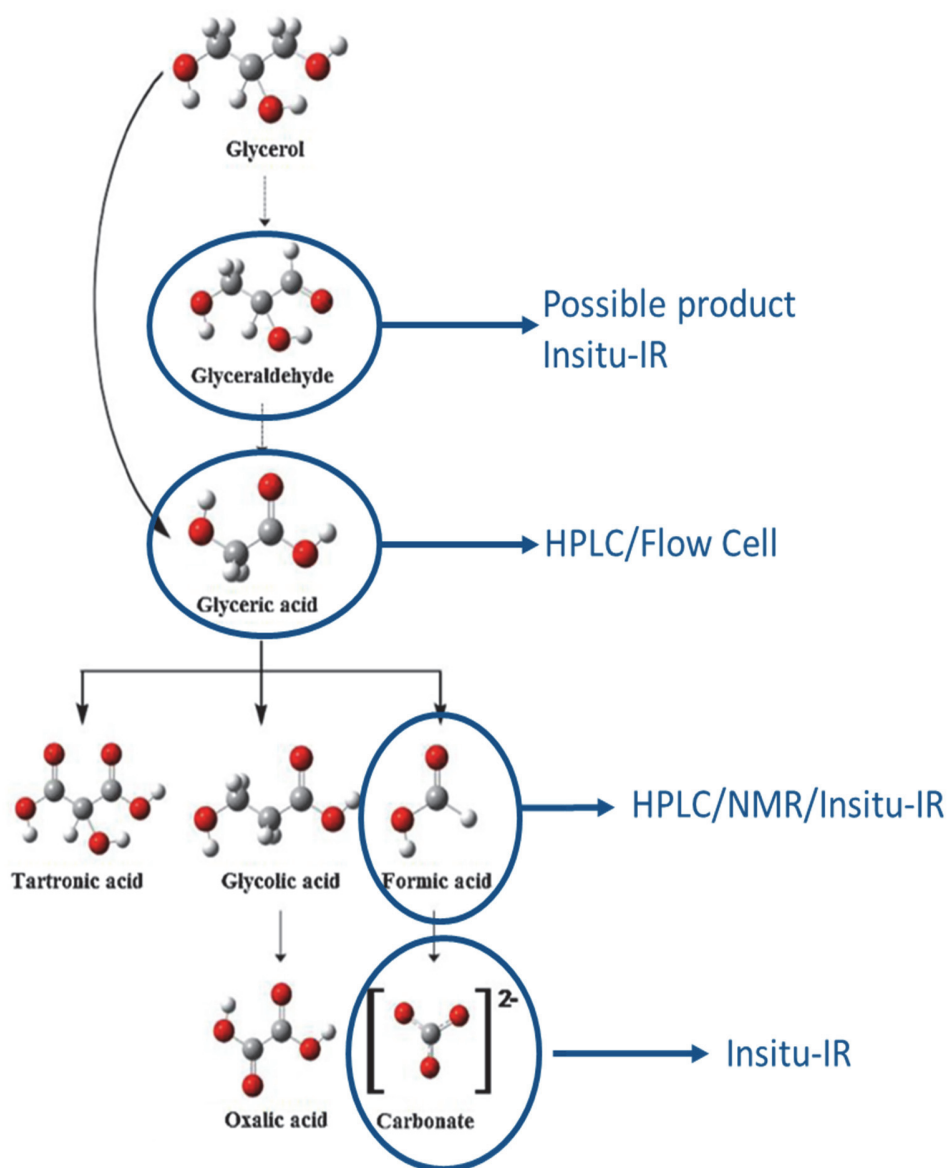


Figure 5.1: Possible reaction scheme for GOR over Co/C-800 catalyst.

6. Future Outlook

During the electrolysis process, the deactivation of the catalyst was one of the major critical issues that needs to be addressed. Modification in the catalyst design to improve its stability would be a possible step forward. Growing the catalyst directly on carbon substrates to improve the mass activity could also be tried. HPLC used for product characterization could be further resolved by varying the column type, temperature and pressure in the HPLC setup. Gradient elution could also be a possible way out.

In this report, we were able to increase the production of C3 product (glyceric acid) by shifting the setup from H-cell to flow-cell. Knowing that GOR is a multistep process the next step would be to use a cascade of flow-through setup with different catalyst material in order to improve product selectivity.

Having an insight into the reaction scheme and catalyst structural characteristics like surface area and average pore diameter required for successful oxidation process; varied catalyst materials can be designed by using different metal combinations and ligands.

References

- [1] T. Covert, M. Greenstone, C. R. Knittel, *J. Econ. Perspect.* **2016**, *30*, 117–138.
- [2] I. P. Jain, *Int. J. Hydrogen Energy*, **2009**, *34*, 7368–7378.
- [3] G. W. Crabtree, M. S. Dresselhaus, M. V. Buchanan, *Phys. Today* **2004**, *57*, 39–44.
- [4] C. L. Choi, J. Feng, Y. Li, J. Wu, A. Zak, R. Tenne, H. Dai, *J. Nano Res.* **2013**, *6*, 921–928.
- [5] S. Trasatti, *J. Electroanal. Chem. Interfacial Electrochem.* **1980**, *111*, 125–131.
- [6] J. Masa, C. Andronescu, H. Antoni, I. Sinev, S. Seisel, K. Elumeeva, S. Barwe, S. Marti-Sanchez, J. Arbiol, B. Roldan Cuenya et al., *ChemElectroChem* **2019**, *6*, 235–240.
- [7] M. R. Monteiro, C. L. Kugelmeier, R. S. Pinheiro, M. O. Batalha, A. da Silva César, *Renewable Sustainable Energy Rev.* **2018**, *88*, 109–122.
- [8] N. Razali, A. Z. Abdullah, *Appl. Catal., A: General* **2017**, *543*, 234–246.
- [9] Y. Kwon, K. J. P. Schouten, M. T. M. Koper, *ChemCatChem* **2011**, *3*, 1176–1185.
- [10] Y. Wang, L. Li, L. Hu, L. Zhuang, J. Lu, B. Xu, *Electrochem. Commun.* **2003**, *5*, 662–666.
- [11] M. Simões, S. Baranton, C. Coutanceau, *Appl. Catal., B* **2010**, *93*, 354–362.
- [12] C. Dai, L. Sun, H. Liao, B. Khezri, R. D. Webster, A. C. Fisher, Z. J. Xu, *J. Catal.* **2017**, *356*, 14–21.
- [13] E. Antolini, *Catalysts* **2019**, *9*, 980.
- [14] C. Coutanceau, S. Baranton, R. S. B. Kouamé, *Front. Chem.* **2019**, *7*, 100.
- [15] Y. Kwon, M. T. M. Koper, *Anal. Chem.* **2010**, *82*, 5420–5424.
- [16] a) Y. Kwon, K. J. P. Schouten, M. T. M. Koper, *ChemCatChem* **2011**, *3*, 1176–1185; b) M. Simões, S. Baranton, C. Coutanceau, *Appl. Catal., B* **2011**, *110*, 40–49; c) M. Simões, S. Baranton, C. Coutanceau, *ChemSusChem* **2012**, *5*, 2106–2124.
- [17] R. G. Da Silva, S. Aquino Neto, K. B. Kokoh, A. R. de Andrade, *J. Power Sources* **2017**, *351*, 174–182.
- [18] P. S. Fernández, M. E. Martins, G. A. Camara, *Electrochim. Acta* **2012**, *66*, 180–187.
- [19] S. Carrettin, P. McMorn, P. Johnston, K. Griffin, G. J. Hutchings, *Chem. Commun.* **2002**, 696–697.
- [20] A. C. Garcia, Y. Y. Birdja, G. Tremiliosi-Filho, M. T.M. Koper, *J. Catal.* **2017**, *346*, 117–124.
- [21] K. Cheung, W. Wong, D. Ma, T. Lai, K. Wong, *Coord. Chem. Rev.* **2007**, *251*, 2367–2385.
- [22] a) J. L. Bott-Neto, T. S. Martins, S. A. S. Machado, E. A. Ticianelli, *ACS Appl. Mater. Interfaces* **2019**, *11*, 30810–30818; b) Q. Lin, Y. Wei, W. Liu, Y. Yu, J. Hu, *Int. J. Hydrogen Energy* **2017**, *42*, 1403–1411; c) M. Gong, H. Dai, *Nano Res.* **2015**, *8*, 23–39.
- [23] V. L. Oliveira, C. Morais, K. Servat, T. W. Napporn, G. Tremiliosi-Filho, K. B. Kokoh, *J. Electroanal. Chem.* **2013**, *703*, 56–62.

- [24] V. L. Oliveira, C. Morais, K. Servat, T. W. Napporn, G. Tremiliosi-Filho, K. B. Kokoh, *Electrochim. Acta* **2014**, *117*, 255–262.
- [25] a) R. Poreddy, C. Engelbrekt, A. Riisager, *Catal. Sci. Technol.* **2015**, *5*, 2467–2477; b) G. Dodekatos, H. Tüysüz, *ChemCatChem* **2017**, *9*, 610–619.
- [26] C. Liu, M. Hirohara, T. Maekawa, R. Chang, T. Hayashi, C.-Y. Chiang, *Appl. Catal., B* **2020**, *265*, 118543.
- [27] J. C. Myland, K. B. Oldham, *Anal. chem.* **2000**, *72*, 3972–3980.
- [28] X.-Z. Yuan, *Electrochemical impedance spectroscopy in PEM fuel cells. Fundamentals and applications*, Springer, London, **2010**.
- [29] a) L.A. Bromley, *AIChE J.* **1973**, *19*, 313–320; b) M. Knobel, *J. Am. Chem. Soc.* **1923**, *45*, 70–76.
- [30] H. B. Aiyappa, P. Wilde, T. Quast, J. Masa, C. Andronescu, Y.-T. Chen, M. Muhler, R. A. Fischer, W. Schuhmann, *Angew. Chem. Int. Ed.* **2019**, *58*, 8927–8931.
- [31] M. B. C. de Souza, R. A. Vicente, V. Y. Yukuhiro, C. T. G. V. M. T. Pires, W. Cheuquepán, J. L. Bott-Neto, J. Solla-Gullón, P. S. Fernández, *ACS Catal.* **2019**, *9*, 5104–5110.
- [32] S. Mortazavi-Derazkola, S. Zinatloo-Ajabshir, M. Salavati-Niasari, *RSC Adv.* **2015**, *5*, 56666–56676.
- [33] J. F. Gomes, C. A. Martins, M. J. Giz, G. Tremiliosi-Filho, G. A. Camara, *J. Catal.* **2013**, *301*, 154–161.
- [34] H. Wang, F.X. Yin, B.H. Chen, X.B. He, P.L. Lv, C.-Y. Ye, D.-J. Liu, *Appl. Catal., B* **2017**, *205*, 55–67.
- [35] X. Li, Z. Niu, J. Jiang, L. Ai, *J. Mater. Chem. A* **2016**, *4*, 3204–3209.
- [36] Flemming A. Andersen, Ljerka Brecevic, *Acta Chem. Scand.* **1991**, *45*, 1018–1024.
- [37] Demetrios Kyriacou, Terrence P. Tougas, *J. Am. Chem. Soc.* **1987**, *52*, 2319–2323.
- [38] Mika Pettersson, Jan Lundell, Leonid Khriachtchev, Markku Räsänen, *J. Am. Chem. Soc.* **1997**, *119*, 11715–11716.
- [39] Y. Kobashi, T. Igarashi, H. Takahashi, K. Higasi, *J. Mol. Struct.* **1976**, *35*, 85–99.

Appendix

Below are the calibration curves of HPLC chromatograms for GLA and FA

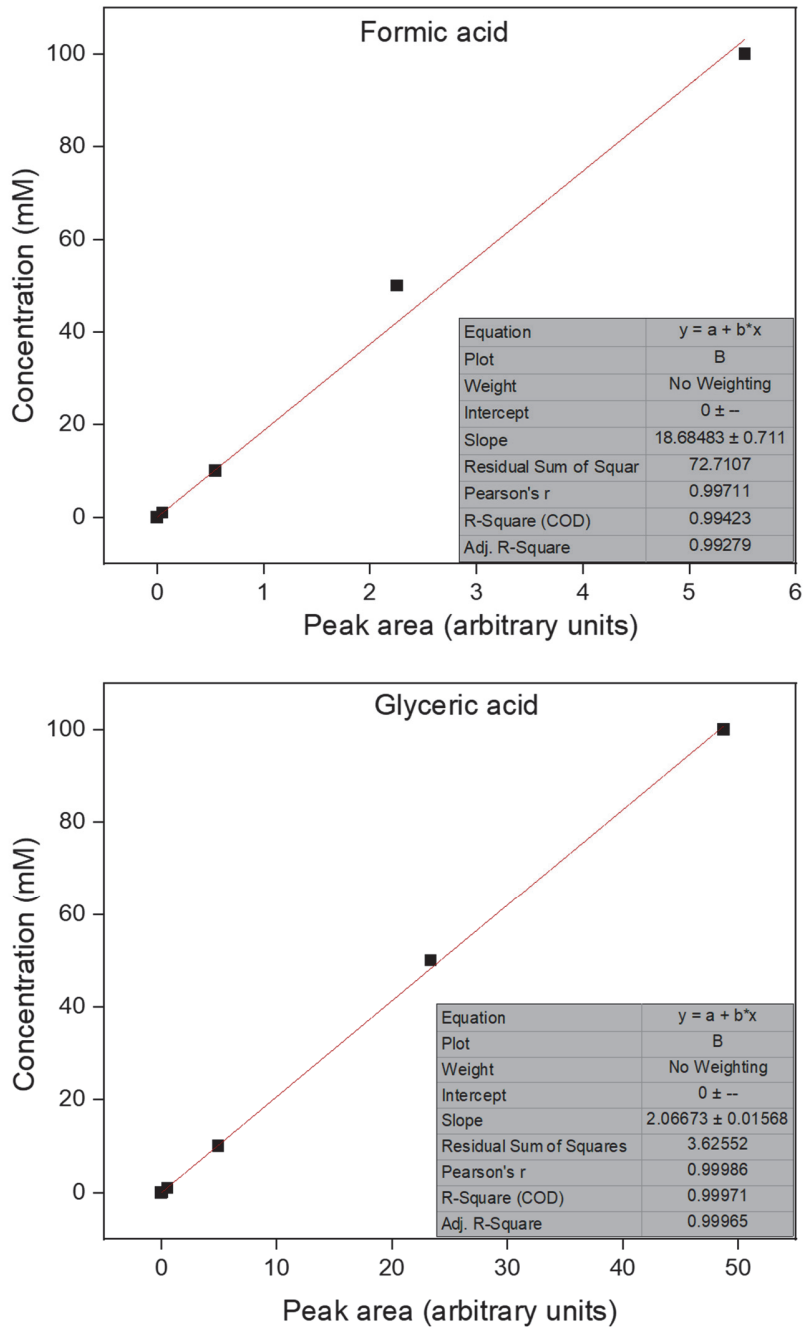


Figure A1: Calibration plots for concentration determination from HPLC chromatograms (a) FA, (b) GLA

¹H NMR reference data for glycerol and few expected products

Analyte	Multiplicity	Chemical shift (ppm)
Glycerol	Multiplet	4.70, 3.71, 3.53
Formic acid	Singlet	8.22
Glyceric acid	Singlet	3.78
Glycolic acid	Singlet	4.11
Lactic acid	Doublet	1.33
